

One-point fluctuation analysis of the high-energy neutrino sky

Michael R. Feyereisen,^a Irene Tamborra^{b,a} and Shin'ichiro Ando^a

^aGRAPPA Institute, University of Amsterdam, Science Park 904, 1098 XH Amsterdam, Netherlands

^bNiels Bohr International Academy, Niels Bohr Institute, Blegdamsvej 17, 2100 Copenhagen, Denmark

E-mail: m.r.feyereisen@uva.nl, tamborra@nbi.ku.dk, s.ando@uva.nl

Abstract. We perform the first one-point fluctuation analysis of the high-energy neutrino sky. This method reveals itself to be especially suited to contemporary neutrino data, as it allows to study the properties of the astrophysical components of the high-energy flux detected by the IceCube telescope, even with low statistics and in the absence of point source detection. Besides the veto-passing atmospheric foregrounds, we adopt a simple model of the high-energy neutrino background by assuming two main extra-galactic components: star-forming galaxies and blazars. By leveraging multi-wavelength data from *Herschel* and *Fermi*, we predict the spectral and anisotropic probability distributions for their expected neutrino counts in IceCube. We find that star-forming galaxies are likely to remain a diffuse background due to the poor angular resolution of IceCube, and we determine an upper limit on the number of shower events that can reasonably be associated to blazars. We also find that upper limits on the contribution of blazars to the measured flux are unfavourably affected by the skewness of the blazar flux distribution. One-point event clustering and likelihood analyses of the IceCube HESE data suggest that this method has the potential to dramatically improve over more conventional model-based analyses, especially for the next generation of neutrino telescopes.

Keywords: Neutrino astronomy, ultra high-energy photons and neutrinos, gamma-ray theory, particle acceleration.

Contents

1	Introduction	2
2	Distributional models of neutrino fluxes	2
2.1	Star-forming galaxy fluxes from the <i>Herschel</i> data	3
2.1.1	Flux model	3
2.1.2	Flux distribution	4
2.2	Blazar fluxes from the <i>Fermi</i> 2FHL catalogue	5
2.2.1	Gamma-ray flux model	6
2.2.2	Neutrino flux model	6
2.2.3	Flux distribution	7
2.3	Atmospheric (cosmic ray) foregrounds	7
3	Flux and count distributions of single pixels	8
3.1	Size of a single pixel	9
3.2	Obtaining the total (multi-source) flux distribution	10
3.2.1	Formalism	10
3.2.2	Discussion	11
3.3	Obtaining the observed count distribution	13
3.3.1	Formalism	13
3.3.2	Discussion	14
4	Analysis (I): Methodology	15
4.1	Resolvability of point sources	15
4.2	A “Pointless” clustering analysis	16
4.3	Single-pixel Likelihood Analysis	17
4.4	Digression on p -values	18
5	Analysis (II): Results	19
5.1	Detectability of star-forming galaxies and blazars as point sources	19
5.1.1	Star-forming galaxies	20
5.1.2	Blazars	22
5.2	Clustering analysis	22
5.3	One-point fluctuation analysis	24
5.3.1	Results	24
5.3.2	Discussion	25
6	Analysis (III): Discussion of systematics	26
6.1	Methodological systematics	26
6.2	Marginalisation systematics	27
6.3	Astrophysical model systematics	28
7	Conclusions	28

A	Modeling of the IceCube effective area	29
A.1	Convolute integration and neutrino fluxes	30
A.2	Declination dependence	32
A.3	Flavour dependence	32
B	Methodological contrast to one-point fitting	32

1 Introduction

In 2013, the IceCube Collaboration reported an excess of high-energy neutrinos over the atmospheric neutrino background [1–5]. The spatial distribution of these events, consistent with isotropy and with no significant clustering, may suggest an extragalactic origin of the detected neutrinos [6–9]. Besides a Galactic contribution [10, 11], various extragalactic astrophysical sources have been suggested as factories of the IceCube neutrinos, e.g. star-forming galaxies (SFG) [12–19], active-galactic nuclei [20–28], galaxy clusters [29, 30], sources dim or scarcely visible in photons [31–37] as well as more exotic dark matter decays [38–41]. Recent work employing accurate statistical analysis as well as up-to-date gamma-ray data-sets places strong constraints on some of the proposed sources [42–45]. In this study we are interested in the joint contribution of multiple source populations to the observed extragalactic neutrino flux.

Given the paucity of the high-energy neutrino data, it is important to extract as much information as we can from them. We here aim at exploiting the full probability distribution of the currently available neutrino data-set by employing a one-point fluctuation analysis [46–51]. We first model the high-energy neutrino sky in a simple data-driven way, by assuming that neutrinos from SFGs and from blazars constitute the main bulk of the observed IceCube flux, other than the atmospheric background. The IceCube HESE data are then compared directly to our model predictions. Our one-point analyses show that the specific model of SFGs and blazars, carefully extrapolated from *Herschel* and *Fermi* data, is insufficient to explain the IceCube astrophysical excess. Our likelihood analysis suggests that the discrepancy can be explained by missing un-modelled components that are likely of astrophysical origin.

In addition to our analysis of the HESE data, the probability distribution of the individual neutrino counts allows us to make detection forecasts of these astrophysical populations as point sources above diffuse backgrounds that they themselves generate. This extreme-value analysis suggests that a detector with the IceCube angular resolution would not be likely to detect SFGs as point sources above the background of blazars and of other SFGs. On the other hand, blazars are sufficiently rare sources that they will not constitute a background to themselves. Instead, the skewness of the blazar flux distribution biases results derived from population averages by a non-negligible factor compared to the full distributional result, which we compute.

The paper is organised as follows. In Sec. 2, we present our data-driven modelling of the extragalactic and atmospheric neutrino flux. In Sec. 3, we predict what IceCube should observe on Earth as a consequence of the adopted astrophysical models and characterise the flux distributions of star-forming galaxies and blazars, arguing that they are sufficiently skewed to bias results on unresolved source contributions to the diffuse backgrounds. In Sec. 4 we present a few of the techniques available in one-point analyses, and in Sec. 5, we apply these techniques and expose the results of our analyses. The systematics of this study are discussed in Sec. 6, and our findings are summarised in Sec. 7. Further materials complementing the methodological discussions are reported in the Appendices.

2 Distributional models of neutrino fluxes

In this Section we describe the inputs we used to model the neutrino emission from SFGs and blazars. We also derive the flux probability distributions of single sources drawn randomly from these populations.

In this study we will consider the energy-differential particle fluxes F (in units of $\text{cm}^{-2} \text{s}^{-1} \text{GeV}^{-1}$) of various sources. Specifically, we will be considering the statistics of the flux in individual pixels, and to some extent we will be treating fluxes-per-pixel as equivalent to intensities $I = F/\Omega_{\text{pix}}$ (in units of $\text{cm}^{-2} \text{s}^{-1} \text{sr}^{-1} \text{GeV}^{-1}$).

In addition to these energy-differential quantities, the gamma-ray studies we use to inform our models often work with fluxes S_γ (in units of $\text{cm}^{-2} \text{s}^{-1}$) integrated over a certain energy range $[E_{\text{min}}, E_{\text{max}}]$. Integrated neutrino fluxes S_ν will also be relevant in Sec. 3.3.1. For a differential flux with fixed spectral index Γ (i.e., $F \propto E^{-\Gamma}$), S is related to F by

$$S = F \times \frac{E_{\text{max}}^{1-\Gamma} - E_{\text{min}}^{1-\Gamma}}{(1-\Gamma) E^{-\Gamma}} . \quad (2.1)$$

Hence, when the spectral index over this energy range is known, F and S are also effectively interchangeable, and we can extrapolate GeV gamma-ray fluxes to their TeV–PeV gamma-ray counterparts. From here we can further extrapolate their corresponding neutrino fluxes assuming pp or $p\gamma$ interactions. Note that we will assume a single injection spectral index Γ as representative of the whole source population for simplicity. In Sec. 6.2, we will discuss the systematics incurred by employing such an approximation. Notational preferences for F , S , or I throughout the text are mainly to emphasise whether or not we are assuming a fixed pixel size (I), a fixed energy range (S), or neither (F).

2.1 Star-forming galaxy fluxes from the *Herschel* data

We now introduce our model for the neutrino emission from star-forming galaxies. The probability distribution of their neutrino flux is also discussed.

2.1.1 Flux model

In a proton-rich astrophysical environment, the neutrino emission can be directly correlated to the gamma-ray emission [6, 52]:

$$\frac{1}{3} \sum_{\alpha=1}^6 E_\nu Q_{\nu,\alpha} = \frac{\kappa}{2} E_\gamma Q_\gamma , \quad (2.2)$$

where α runs over (anti)neutrino flavours, Q is the energy-differential emission rate per source (in units of $\text{s}^{-1} \text{GeV}^{-1}$) and $\kappa = 2$ for hadro-nuclear interactions. Using the direct relation between the neutrino and the gamma-ray energies ($2E_\nu = E_\gamma$) and integrating over source densities on both sides of Eq. (2.2) to get the differential fluxes (in units of $\text{cm}^{-2} \text{s}^{-1} \text{GeV}^{-1}$), we have $(1/6) \sum_\alpha F_{\nu,\alpha} = (\kappa/2) F_\gamma$. Since neutrino oscillations push the flavour ratio towards 1:1:1 for extragalactic sources, we can define the all-flavour neutrino and antineutrino flux as

$$F_\nu \equiv \sum_{\alpha=1}^6 F_{\nu,\alpha} = 3\kappa F_\gamma . \quad (2.3)$$

Although we have a simple conversion between neutrino and gamma-ray fluxes for hadronic sources, SFGs are barely resolved in gamma rays (cf. e.g. [53–56]). Consequently, their neutrino flux distribution is derived following Ref. [16]. We adopt the *Herschel* infrared (IR) luminosity function, $\Phi(L_{\text{IR}}, z) = d^2N/(dV(z) d\log_{10} L_{\text{IR}})$ [57], defined for the intrinsic infrared luminosity L_{IR} and redshift z . The IR luminosity function is connected to the

gamma-ray luminosity function $\Phi(L_\gamma, z)$ by an empirical correlation [53]

$$\Phi_\gamma(L_\gamma, z)d\log L_\gamma = \Phi_{\text{IR}}(L_{\text{IR}}, z)d\log L_{\text{IR}} , \quad (2.4)$$

$$L_\gamma(L_{\text{IR}}) = 10^\beta \left(\frac{L_{\text{IR}}}{10^{10}L_\odot} \right)^\alpha \text{ erg s}^{-1} , \quad (2.5)$$

where $\alpha = 1.17 \pm 6\%$ and $\beta = 39.28 \pm 0.2\%$ and L_\odot is the solar luminosity. We will assume the best fit values of the above parameters in the following, though more rigorously we really should be marginalising over these uncertainties. The 0.2% uncertainty on the normalisation exponent β corresponds to an 18% systematic uncertainty on the normalisation 10^β . Meanwhile the uncertainty on the slope corresponds to a $\lesssim 2\%$ uncertainty on the normalisation for the values of L_{IR} at the edges of the domain of $\Phi(L_{\text{IR}})$ [57], and is correlated with L_{IR} itself. The combined systematic uncertainty on the extrapolation $L_\gamma(L_{\text{IR}})$ for a single source (and so also on its neutrino flux $F_\nu = 3\kappa F_\gamma$) is then less than $\sim 20\%$. For a further discussion of this systematic effect, see Sec. 6.2.

As discussed in Refs. [16, 57], the luminosity function of IR galaxies can be decomposed into luminosity functions for spiral (‘normal’) galaxies (NG), starburst galaxies (SB), and star-forming galaxies hosting an obscured or low-luminosity AGN (SF-AGN). This last subpopulation is further divided into those having an energy spectrum resembling the one of normal galaxies (SF-AGN (NG)) and those more similar to starburst galaxies (SF-AGN (SB)); the redshift evolutions of SF-AGNs is given in Table 2 of Ref. [16]. Moreover, SB-like galaxies usually have a harder spectrum than NGs ($\Gamma_{\text{SB}} \simeq 2.2$ vs. $\Gamma_{\text{NG}} \simeq 2.7$, see Ref. [16, 44] and references therein for more details). In the following, we will only consider SB and SF-AGN (SB) galaxies as main contributors to the high-energy neutrino flux.

Since SF-AGNs represent the most abundant sub-class of SFGs, we also computed the flux distribution of SF-AGN (NG) as a cross-check ($\Gamma_{\text{SF-AGN(NG)}} = 2.7$). However, we find this subpopulation only produces about 6% of the SFG flux between 25 TeV and 5 PeV, well within systematic uncertainties, so this subpopulation has been neglected in what follows.

We assumed the energy-dependence of the γ -ray differential flux as an unbroken power-law $\propto E^{-\Gamma_{\text{SB}}}$ above 0.6 GeV [16] and do not adopt an high-energy cutoff. We will further discuss the effect of uncertainties on Γ in Sec. 6.2.

2.1.2 Flux distribution

For an SFG population composed of exactly $N = \int (dV/dz)\Phi(L_\gamma, z)d\log L_\gamma dz$ sources, the luminosity function is sufficient (under the assumption that these extragalactic sources are isotropically distributed in a comoving cosmological volume element dV/dz) to obtain the single source distribution:¹

$$P_1(L_\gamma, z) = \frac{d^2N/dz dL_\gamma}{N} = \frac{dV}{dz} \frac{\Phi_\gamma(L_\gamma, z)}{N \ln(10)L_\gamma} . \quad (2.6)$$

We use the Planck+WMAP cosmology in dV/dz ($h = 0.673$, $\Omega_\Lambda = 0.685$, $\Omega_m = 0.313$) [58].

For a population with a unique, fixed spectral index Γ and photons observed at energy E_γ (i.e., emitted at various energies $(1+z)E_\gamma$), the one-source gamma-ray differential flux

¹Throughout this paper, we denote probability distributions by $P(\dots)$ and distinguish them using the random variables that they describe, along with subscripts if necessary. Conditional and parameterised distributions are denoted as $P(\cdot|\cdot)$. The ‘exception’ to this convention is the Poisson distribution, denoted $\mathcal{P}(\cdot)$.

distribution is obtained by marginalising away the uncertainties on the (L_γ, z) of the source:

$$P_1(F_\gamma|E_\gamma, \Gamma) = \iint dz dL P_1(F_\gamma, L_\gamma, z|(1+z)E_\gamma, \Gamma) = \int dz \left| \frac{L_{\text{crit}}}{F_\gamma} \right| P_1(L_{\text{crit}}, z), \quad (2.7)$$

where $L_{\text{crit}}(F_\gamma, E_\gamma, \Gamma, z)$ is the L_γ value obtained by the inversion of the differential flux model $F_\gamma(L_\gamma, \dots)$ from Ref. [16] in which any attenuation during propagation is neglected. Inserting Eqn. (2.6) then yields

$$P_1(F_\gamma|E_\gamma, \Gamma) = \frac{1}{|F_\gamma|} \int dz \frac{dV}{dz} \frac{\Phi_\gamma(L_{\text{crit}}, z)}{N \ln(10)}, \quad (2.8)$$

where uncertainties of $\Gamma_{\text{SB}} = 2.2$ are explicitly neglected. The effect of systematic uncertainties of Γ on the mean flux in such a model has already been studied in Ref. [16], and the systematic effects of statistical uncertainties on Γ are discussed in Sec. 6.2. The SFG normalisation N is effectively absorbed into the normalisation $\int dP = 1$ of this single-source probability distribution, although it remains determined by the *Herschel* observations when we extrapolate this gamma-ray flux to neutrinos using Eqn. (2.3).

For the high-flux tail, with contributions only from the nearby sources, the volume probed is very small and we expect an Euclidean scaling $F^{-2.5}$. The resulting $P_1(F_\nu)$ is then a broken power-law, up to corrections due to the redshift evolution of the SFG populations [57], as visible in Figure 1.

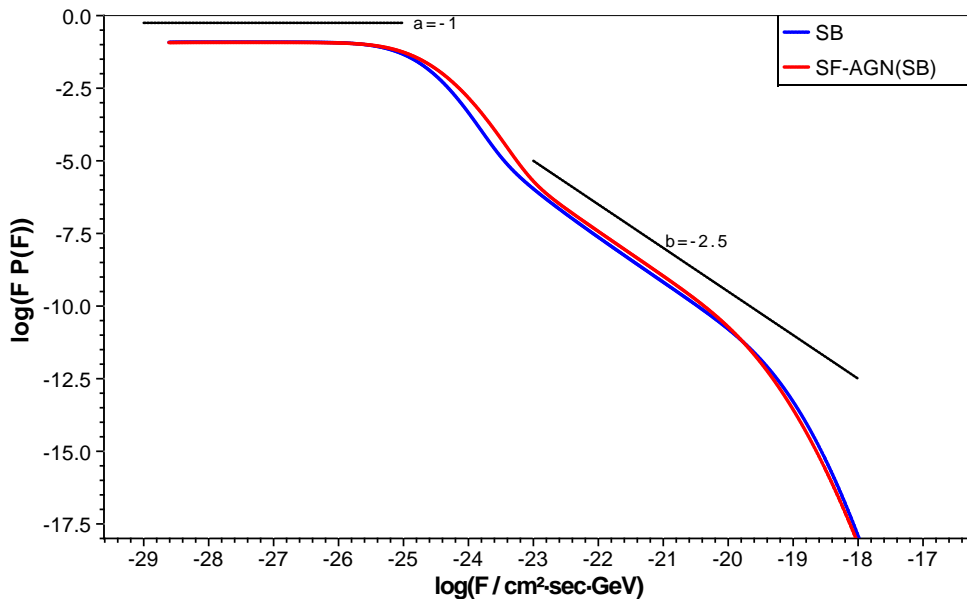


Figure 1: Probability distribution $P_1(F_\nu)$ of the differential neutrino flux from a single star-forming galaxy at 100 TeV. The flux distributions of two SFG subpopulations are shown: SB (blue) and SF-AGN (red) [16]. Constant log-slopes corresponding to the limiting $1/|F|$ and the Euclidean behaviours (a and b respectively) are offset and quantified for convenience.

2.2 Blazar fluxes from the *Fermi* 2FHL catalogue

The second class of extragalactic neutrino sources in our model are blazars. In what follows we introduce our model to estimate their neutrino emission the basis of based on their observed γ -rays spectra. The probability distribution of their flux is briefly introduced.

2.2.1 Gamma-ray flux model

To construct our data-driven model of blazars, we rely on the source count distribution dN/dS_γ of the Second Catalog of Hard *Fermi*-LAT Sources (2FHL) [59, 60]. The 2FHL sources are mostly blazars, specifically BL Lacs. One may justify this claim by extrapolating the observed contributions from different blazar populations at high energy ($\sim 54\%$ BL Lac and $\sim 16\%$ other blazar sub-populations [59]) to the unassociated and unresolved sources. However, before extrapolating this gamma-ray flux into a neutrino flux, we must extrapolate it up to the IceCube energy range.

The 2FHL catalogue has substantially different properties from 2LAC, a 2FGL-based catalogue more commonly used in blazar-neutrino studies [61, 62]. 2LAC is of a higher purity than 2FHL (97% of sources are blazars of various subclassifications); however these sources are observed using gamma-rays at energies 100 MeV – 100 GeV, while the 2FHL is based on data between 50 GeV – 2 TeV [59, 61]. Consequently, extrapolating the gamma-ray flux of 2LAC sources to their neutrino flux above 10 TeV is more dangerous than extrapolating the γ -flux of 2FHL sources.

This is relevant because the spectrum of these sources is very different in the two catalogues. BL-Lacs in the 2LAC have $\Gamma < 2.2$, but appear much softer in the higher energy range of 2FHL. For example, Fig. 10 of Ref. [59] shows the distribution of Γ in a sample of BL Lacs shared between 2FHL and lower energy catalogues, with the clear trend that these sources' indices get softer at increasing energy, with median $\Gamma > 3$ in the 2FHL. This softening is observed despite the larger fraction of HSP ('hard') to LISP ('soft') blazars in 2FHL than in catalogues at lower energies [59], which suggests the unresolved sources we want to model are even softer. This spectral behavior is consistent with the observation that the spectral energy distributions (SEDs) of individual blazars are concave functions. The gamma-ray spectrum approaching PeV energies might be expected to be even softer than those of the 2FHL.

Despite this evidence that the blazar index is $\Gamma > 3$ at higher energies, we nevertheless assume a non-concave SED at high energies, using Eqn. (2.1) with $\Gamma_{2\text{FHL}} = 2.5$. We make this simplifying assumption not only since we expect the flux from a population with uncertain Γ to be dominated by the hardest sources (cf. Sec. 6.2) and for ease of comparison with existing studies (e.g. Refs. [62, 63]), but also because this harder-than-expected extrapolation will result in an optimistic estimate of the contribution from blazars in the 2FHL (and hence in overconservative significances in our one-point fluctuation analyses in Sec. 5). We will further discuss the effect of uncertainties on Γ in Sec. 6.2.

2.2.2 Neutrino flux model

Now that we can extrapolate the gamma-ray flux between 50 GeV – 2 TeV to higher energies, we want to turn it into a neutrino flux. In this case, Eqn. (2.2) does not apply. We adopt instead the following relation from Ref. [25, 64, 65] for the (all-flavors) neutrino flux:

$$E_\nu^2 F_\nu(E_\nu) = \left[\int_{10 \text{ GeV}}^{\infty} E_\gamma F_\gamma dE_\gamma \right] \frac{Y}{0.9} \left(\frac{E_\nu}{E_{\nu,\text{peak}}} \right)^{1-s} \exp\left(-\frac{E_\nu}{E_{\nu,\text{peak}}}\right) \quad (2.9)$$

where $E_{\nu,\text{peak}} \approx 10 \text{ PeV}$ for typical 2FHL sources ($z = 0.4$, $\nu^S = 10^{16} \text{ Hz}$ [59]), and where $s = -0.35$ is used to obtain the denominator factor of 0.9 in the normalisation [25]. Y is a parameter absorbing the details of the particle physics interactions in BL Lacs: the observed gamma-ray flux is mostly leptonic when $Y < 1$, and mostly due to synchrotron emission from

$p\pi$ when $Y \sim 3$. The value $Y = 0.8$ was chosen for ease of comparison with Ref. [25], though their discussions suggests smaller values of Y may be more consistent with IceCube upper limits at the highest energies. This choice of a large Y may therefore slightly overestimate the neutrino flux due to 2FHL sources, which will again result in overconservative significances for the discrepancies between our model and the HESE data we will discuss in Sec. 5.

We can convert the integrated energy flux above 10 GeV in Eqn. (2.9) to the integrated particle flux in the 2FHL energy range, S_γ , using Eqn. (2.1). The term in square brackets above becomes $[\int_{10\text{ GeV}}^\infty E_\gamma F_\gamma dE_\gamma] = S_\gamma(1-\Gamma)/(2-\Gamma)[-(10\text{ GeV})^{2-\Gamma}]/[(2\text{ TeV})^{1-\Gamma} - (50\text{ GeV})^{1-\Gamma}]$. Thus we have

$$F_\nu \propto S_\gamma E_\nu^{-(1+s)} \exp(E_\nu/E_{\nu,\text{peak}}) , \quad (2.10)$$

with a predetermined proportionality constant that depends on the best-fit gamma-ray slope $\Gamma_{2\text{FHL}} = 2.5$ from Ref. [60]. The log-derivative $\partial \ln F_\nu / \partial \ln E_\nu$ gives an energy-dependent neutrino spectrum $F_\nu \propto E_\nu^{-(1+s(E_\nu))}$ which softens as the energy increases, $s(E_\nu) = s + E_\nu/(10\text{ PeV})$. Note that the neutrino spectrum s is different from the gamma-ray spectrum Γ in our phenomenological model. A more accurate modeling of the microphysics may lead to more accurate predictions for s , but this goes beyond the demonstrative scope of our work.

2.2.3 Flux distribution

These extrapolations $S_\gamma^{2\text{FHL}} \rightarrow F_\nu$ are only the first step in determining the probability distribution $P_1(F_\nu|E_\nu)$ of the flux of any single source in the 2FHL. In terms of the number distribution dN/dS_γ of sources resolved by *Fermi* in a flux range $[S_\gamma, S_\gamma + dS_\gamma]$, the single-source flux probability density is

$$P_1(S_\gamma) = \frac{1}{N} \frac{dN}{dS_\gamma} . \quad (2.11)$$

A Monte-Carlo incorporating the *Fermi* detection efficiency was used in Ref. [60] to obtain the intrinsic dN/dS_γ of the 2FHL (i.e., the dN/dS extrapolated below the detection threshold). In this extrapolation the normalisation N is implicitly determined by the faintest-source flux cutoff $S_{\gamma,\text{min}} = 10^{-13} \text{ deg}^{-2} \text{ cm s}$, chosen to self-consistently reproduce the best-fit diffuse flux observed by *Fermi* [60]. This flux distribution, taking the form of a broken power-law, is a data-driven model of these *Fermi* sources, without any attempt at discriminating sub-populations in the catalog and without consideration of the physics which gives rise to these gamma rays. To compute $P_1(F_\nu|E_\nu)$ from $P_1(S_\gamma)$, notice that the flux conversion Eqn. (2.10) is effectively just a linear rescaling of the flux by a known term that depends on energies, on the spectral indices $\Gamma_{2\text{FHL}}$, $s(E_\nu)$, and on the fixed quantities $Y, E_{\nu,\text{peak}}, s(10\text{ PeV})$.

2.3 Atmospheric (cosmic ray) foregrounds

Before continuing our discussion of the flux distributions of extragalactic astrophysical sources, we introduce the atmospheric foregrounds from which these astrophysical contributions must be extricated [2]. Atmospheric neutrinos produce an almost isotropic foreground with a soft spectrum. Our models of the conventional and prompt contributions are based on Ref. [66] and Ref. [67], respectively. We set the probability densities $P^{\text{atm}}(I_\nu|E_\nu)$ of atmospheric all-flavour differential neutrino intensities $I_\nu = F_\nu/\Omega$ to Gaussians.² The finesse of these

²This can be justified, in the spirit of Sec. 3.2.1, by noting that this flux is the result of a very large number of cosmic ray interactions in the atmosphere, such that the central limit theorem may safely be assumed to hold for $P^{\text{atm}}(I_\nu|E_\nu)$.

distributions is chosen as $\mu/\sigma = 10$ (i.e., a 10% intrinsic variability in the atmospheric intensity), the 2σ contours of which are represented as the vertical width around the mean differential intensities in Figure 2.

The means of these distributions are determined as follows. For the conventional contribution, the mean intensity is parameterised as

$$\langle I_\nu(E) \rangle = 2 \times 10^{-14} \left(\frac{E_\nu}{10 \text{ TeV}} \right)^{-\Gamma_\nu} \text{ cm}^{-2} \text{ s}^{-1} \text{ sr}^{-1} \text{ GeV}^{-1}, \quad (2.12)$$

where the normalisation is set by the ν_μ flux at 10 TeV in Ref. [66] and the extra factor of two accounts for the roughly equal flux of muon anti-neutrinos. For the sake of simplicity, we neglect the anisotropic contributions to the atmospheric flux. For the conventional contribution due to ν_μ , this is mainly a zenith dependence at the South Pole (cf. Fig. 7 in Ref. [66]). The spectrum Γ_ν is softer than the cosmic ray primaries by $\Delta\Gamma = 1$. The cosmic ray knee is shifted down to about 1 PeV for neutrinos, such that

$$\Gamma_\nu(E_\nu) = \begin{cases} 3.7 & \text{when } E_\nu < 1 \text{ PeV} \\ 3.9 & \text{when } E_\nu > 1 \text{ PeV} \end{cases}. \quad (2.13)$$

In addition to this neutrino intensity, muon events passing the quality veto of the HESE data (cf. Sec. 3.1 and [2]) were modelled by rescaling the conventional flux by a factor of 4/3, in accordance with the benchmark event rates from the two-year study which claimed ~ 4.5 and 6 events in ν_μ and μ^\pm respectively [2].

As for the prompt atmospheric contribution, we interpolate the average $\nu_\mu + \bar{\nu}_\mu$ flux from Ref. [67] as a function of the energy, and add a rescaling factor of two to account for the roughly equal muon and electron (anti)neutrino fluxes. The enhanced prompt contribution from the proton intrinsic charm [68, 69] is neglected given the opposite shifts in flux from other updated QCD predictions (cf. e.g. [70]), and given the upper limits set in Refs. [5, 63].

The count distribution is then obtained by marginalising the flux distribution into the detector response, with each pixel, energy bin, and event topology treated independently, as will be described in the next section. Convoluting all of these independent distributions gives the predicted distribution of the total number of detected atmospheric neutrinos (and veto-passing muons). The average number of atmospheric counts between 25 TeV and 5 PeV in this model is 27.9. This can be further decomposed into 5.3, 9.7 and 12.9 events from prompt neutrinos, conventional neutrinos, and veto-passing muons, respectively, in rough agreement with an extrapolation of the two-year benchmark rates from Ref. [2] to a four-year lifetime. Poisson shot noise is the dominant source of uncertainty on these event counts, but since we study the fluctuations themselves (statistically), we are in principle sensitive to the assumed $P(I_\nu)$ rather than just the mean $\langle I_\nu \rangle$.

3 Flux and count distributions of single pixels

In order to turn the above astrophysical models into predictions about the data observed by IceCube, we must fold in some detector characteristics (angular resolution, effective area, etc.), which will be described in this section. We also derive the total observed flux and count distributions.

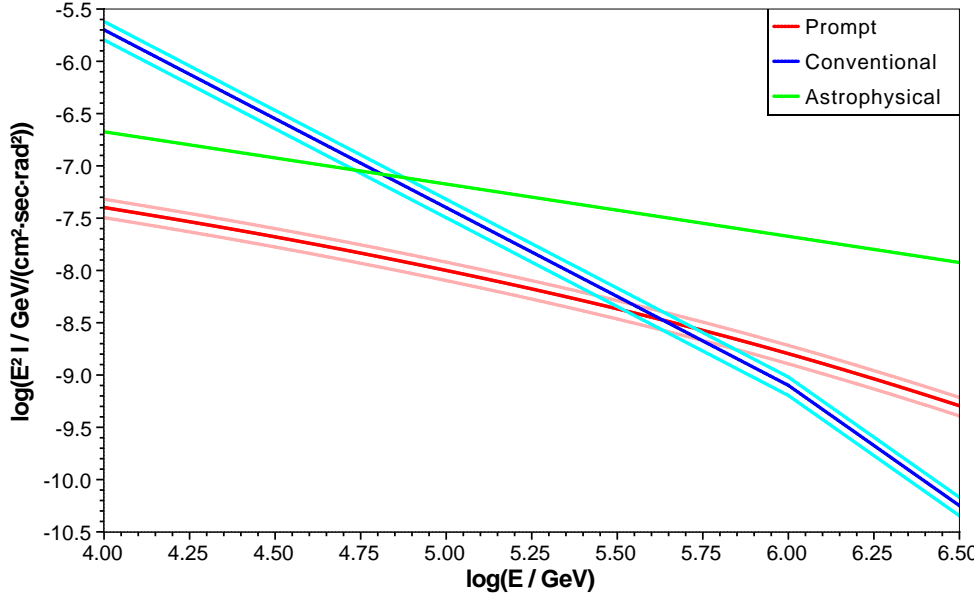


Figure 2: Intensity $E_\nu^2 I_\nu(E_\nu)$ of the conventional (blue) and prompt (red) atmospheric contributions, as a function of energy. The 2σ bands shown here correspond to the intrinsic atmospheric variability $P(I_\nu|E_\nu)$ assumed in this analysis. These contributions are contrasted to the best-fit flux to the IceCube data from Ref. [71] (green). In addition to these neutrino foregrounds, we also consider the veto-passing muon background (cf. main text).

3.1 Size of a single pixel

In our analysis, we try to predict (from the data-driven models discussed above) both IceCube tracks and showers (cascades), with pixel exposures constructed from a flavour, energy, and declination dependent effective area tuned to the HESE dataset [2–4]. This dataset consists of 54 events in the energy range [25 TeV, 5 PeV], with interaction vertices contained within the detector: 39 showers, 14 tracks, and one coincident event not used in this study. Despite the stringent quality cuts, this neutrino dataset remains contaminated by veto-passing muons (cf. Sec. 2.3), which contribute mostly but not exclusively to tracks (cf. Appendix A.3 and Ref. [72]).

Since we are predicting probability distributions per pixel, we will make the simplifying assumption that pixel sizes are constant as a function of the energy: roughly 30 degrees for showers and 1 degree for tracks. These correspond to rough estimates of the median angular resolution of showers [2] and contained tracks [5] at the energies considered in this study (25–5000 TeV). These pixel sizes are used to bin the HESE events into 48 shower pixels and 49152 track pixels, generated using HealPix [73]; these per-pixel counts will be directly compared to the predicted per-pixel count distributions (which include the flavour, energy, and declination-dependent HESE effective area) in Sec. 5. Our study of probability distributions in pixels $\Delta\Omega$ rather than true one-*point* functions, although conceptually simpler, effectively ties us to this binned representation of the data. For a further discussion of binning and Healpix, see Sec. 6.1 and Appendix Sec. A.2.

We emphasise that it is not in principle required to assume an energy-independent angular resolution to compute or study single-pixel fluctuation probabilities. Furthermore, there is no methodological requirement to make pixels of the same scale as the angular

resolution. This choice is mostly for ease of comparison with point source search studies in the literature [4, 5, 43, 52] and our forecasts thereof in Sec. 5.1. Note that pixels must be at least as large as the angular resolution in order to treat their fluxes as independent.

3.2 Obtaining the total (multi-source) flux distribution

So far, we have been considering the flux distribution of a single source drawn at random from its population. However, in observations of abundant sources such as SFGs, there will be many sources in each of IceCube’s pixels. The single-source quantity $P_1(F)$ therefore needs to be promoted to a single-pixel quantity $P(F)$. Here we discuss how to derive the latter from the former, and discuss some features of the blazar and SFG populations’ per-pixel flux distributions.

3.2.1 Formalism

The flux incident on a pixel is the sum of the fluxes of all the sources in that pixel. Given the distribution $P_1(F)$ of the spectral flux per source and the distribution of the number of sources N' in a single given pixel, characterised by the mean $\langle N' \rangle = (\Omega_{\text{pix}}/4\pi)N$, it is straightforward to express the distribution $P(F)$ of the flux in a pixel in terms of the distribution $P(F|N')$ of the sum of the fluxes of N' sources:

$$P(F) = \int P(F|N')P(N'|\langle N' \rangle)dN'. \quad (3.1)$$

By independence of the sources and the algebra of random variables, the distribution of the sum of their fluxes is given by the auto-convolution

$$P(F|N') = \underbrace{P_1(F) \star P_1(F) \star \cdots \star P_1(F)}_{N' \text{ times}}, \quad (3.2)$$

where $f \star g$ denotes the convolution of the two probability distributions f, g .

The marginalised auto-convolution is as difficult to calculate as it is straightforward to express, since the Fourier space techniques usually applied to such compound Poisson distributions [74] develop numerical instabilities for power-law-like $P_1(F)$ spanning many orders of magnitude. We adopt instead the following Monte-Carlo strategy [46]:

- When the average number of sources per pixel $\langle N' \rangle$ is too large to sample from $P_1(F_\nu)$ tails efficiently, we use the Central Limit Theorem to lump the faint sources into a diffuse Gaussian background and consider only the few brightest sources in that pixel.
- When the average number of (bright) sources per pixel is small, we can repeatedly (i) realise this number N' from a Poisson distribution with the mean $\langle N' \rangle$, (ii) draw that many samples from the single-source flux distribution, and (iii) add them all up. The histogram of the sums of fluxes approximates $P(F)$.

In addition, the highest fluxes of $P(F)$ are known to converge to $P_1(F)$ [46], which can be used to supplement the Monte-Carlo-derived $P(F)$ with an analytical “bright point-source” tail. Realising N' from a Poisson distribution without marginalising over any uncertainties in $\langle N' \rangle$ effectively suppresses the variance of the statistically isotropic flux (cf. Sec. 6.1), to which one-point methods are sensitive as a signal rather than a background [75, 76].

3.2.2 Discussion

By applying Eqn. (3.2) to the SFG single-source flux distribution, we plot in the top panel of Fig. 3 the probability distribution $P(I_\nu)$ of the SFGs at 100 TeV for tracks and showers. Note that the distributions have the form of a Gaussian with a power-law tail. These features correspond to the diffuse glow of a large number of unresolved point sources, and to the few point sources with intensities high enough to potentially be resolved individually [46]. We postpone discussion of point-source-detectability prospects for these populations until Sec. 5. Here we focus on the physical interpretation and consequences of the features of $P(F_\nu)$.

Although the single-source flux distribution is independent of the normalisation of the SFG luminosity function, the total flux distribution is sensitive to this normalisation via the average number $\langle N' \rangle$ of sources per pixel. The uncertainties on the normalisations of the SB and SF-AGN (SB) luminosity functions are not formally considered as distributions to be marginalised away in this study. However, we discuss these uncertainties below and in Sec. 6.2.

The mean and variance of $P(F_\nu)$ are nothing other than a linear rescaling of the mean and variance of $P_1(F_\nu)$ by a factor of $\langle N' \rangle$. For example, the relative locations of the SFG subpopulations in Fig. 3 are determined by the combination of two effects: firstly, there are roughly $(25 \pm 15)\%$ more members of the SF-AGN (SB) subpopulation than of the SB subpopulation in each pixel (according to the normalisations of the *Herschel* luminosity functions used in Sec. 2.1.1); secondly, and more importantly, the mean flux of an individual SF-AGN (SB) is larger than the mean flux of an SB (consider Fig. 1 between 10^{-25} and 10^{-20} $\text{cm}^{-2} \text{s}^{-1} \text{GeV}^{-1}$). These two effects push the typical flux per pixel from SF-AGN (SB) sources slightly above that of SB sources in our model.

Moreover, we expect that the peak finesse increases with $\langle N' \rangle$, as a consequence of the $\sqrt{\langle N' \rangle}$ scaling of the finesse in the central limit theorem that gives a Gaussian shape to the diffuse peak [46]. This can be corroborated by looking, in Fig. 3 or in Table 1, at the same populations in tracks and in showers: tracks have a better angular resolution and therefore wider diffuse peaks because $\langle N' \rangle$ drops from $\mathcal{O}(10^6)$ to $\mathcal{O}(10^3)$ in both SB and SF-AGN (SB). A linear regression of the finesse of diffuse peaks from the four $P(F)$ distributions of Fig. 3 on their respective $\sqrt{\langle N' \rangle}$ yields a Pearson $R^2 = 0.999$.

The locations of the peaks of these distributions are also slightly offset among each other, the peak in showers is at slightly higher flux than the peak in tracks (again, as visible in Fig. 3 or in Table 1). This is also a consequence of convergence in the central limit theorem. Indeed, the single-source distribution is power-law like and hence very skewed, but the more sources we have in our pixel, the less we are dominated by the individual source properties and the closer we get to the population mean intensity—which is a quantity dependent on the luminosity function, but independent on the angular resolution. Since showers contain more unresolved sources than tracks, the diffuse peak in showers is closer to the mean of these distributions than the diffuse peak in tracks.

The flux distribution for 2FHL sources in showers (bottom panel of Fig. 3) is qualitatively similar to the flux distributions of SFGs (top panel of the same figure), though its power-law tail is much more prevalent; there are few enough sources per pixel ($\langle N' \rangle = 429$) that even the diffuse peak is distinctly skewed. This non-Gaussianity can, in principle, be exploited to characterise diffuse backgrounds from unresolved sources, even though source number density and source luminosity are degenerate at the level of averages [43]. The small number of sources per pixel also means that the 2FHL peak is much wider than the SFG

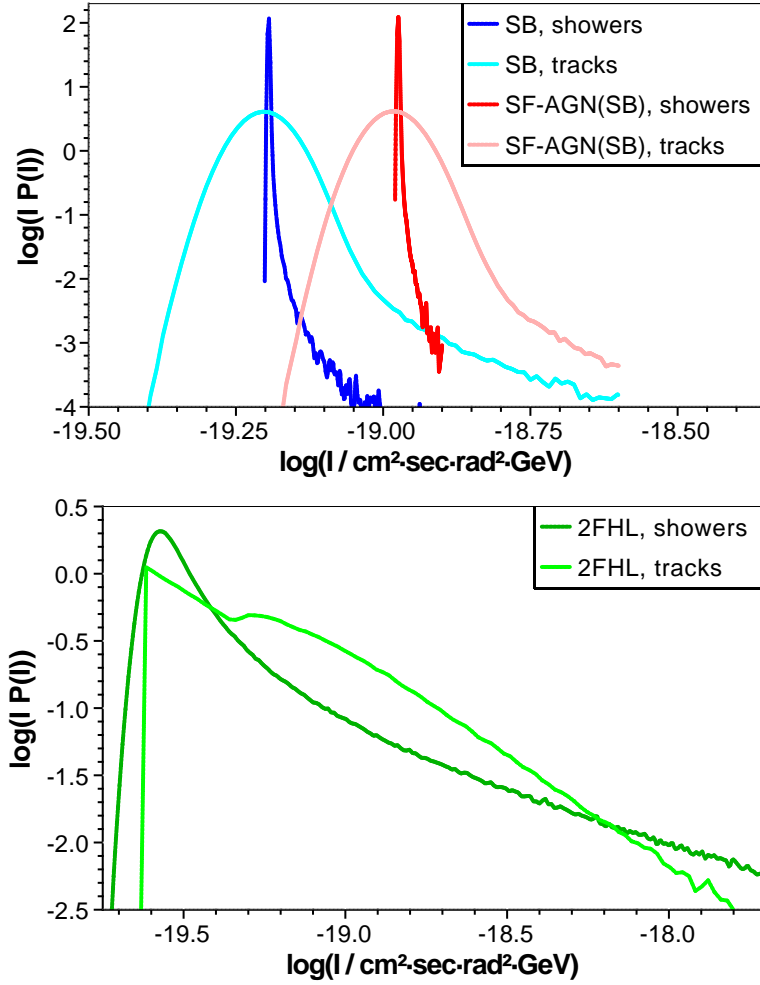


Figure 3: *Top:* Probability distribution $P(I_\nu)$ of the SFG intensities as observable at 100 TeV. These distributions take the form of a Gaussian peak with a power-law tail. Starbursts are shown in blue (showers) and cyan (tracks), while SF-AGN (SB) are shown in red (showers) and pink (tracks). In each subpopulation, these peaks are much thinner in showers than in tracks as a consequence of the increased number of sources in larger pixels (cf. main text). *Bottom:* Probability distribution $P(I_\nu)$ of 2FHL source intensities at 100 TeV, in showers (dark green) and tracks (light green). These distributions are shown conditioned on there actually being a blazar in the pixel, so the absolute and relative normalisations are not visible in this figure. The cusp in tracks occurs at twice the minimum flux, it is the transition from one to two sources per pixel. Above this cusp, multiple sources contribute jointly to the flux, and a smooth bump begins to form.

peaks, by a factor exceeding an order of magnitude (cf. Table 1). This further corroborates the theoretically expected $\sqrt{\langle N' \rangle}$ scaling of the finesse.³

The 2FHL distribution in tracks is informed by the tiny number of sources per pixel ($\langle N' \rangle = 0.42$) and the sharp cutoff imposed at lower fluxes in the single-source distribution

³Although this scaling is a useful tool within a single population of unresolved sources, across multiple source populations other population-specific factors come into play and the explained variance R^2 decreases.

in Sec. 2.2.3. The cusp in the bottom panel of Fig. 3, located at twice the minimum flux, corresponds to the discrete transition from one to two sources per pixel, and below this cusp the distribution is accordingly a pure power law (corresponding to a single source). Above this cusp, multiple sources contribute jointly to the flux, and a smooth bump begins to form; this bump becomes the diffuse peak when the pixel size increases. The power-law tail sets in at higher flux when one of the blazars dominates the flux of the others. As in the case of SFGs, the most likely flux for tracks is still at smaller flux than for showers.

3.3 Obtaining the observed count distribution

The neutrino fluxes produce discrete event counts in our detector. Having a detector model built into our pipeline means that we can compare the distributional predictions of our astrophysical models directly to the raw event count data in terms of count distributions $P(C)$.

3.3.1 Formalism

At the bare minimum, a detector model consists of a pixel’s exposure and solid angle. Having already accounted for the latter, the exposure can be constructed by multiplying the IceCube livetime (roughly four years with a 95% duty cycle) by its effective area A , which is flavour, energy, and declination dependent [2–4]. We postpone discussion of the flavour and declination dependence to the Appendices, and focus here on our distributional treatment of the energy dependence.

Using Eqn. (2.1) to convert from differential neutrino fluxes F_ν into integrated neutrino fluxes S_ν , the distribution $P(S_\nu)$ (integrated over an energy bin $[E_{\nu,\min}, E_{\nu,\max}]$) can be made into a number of counts per pixel and per energy bin, by marginalising the flux distribution into the detector response, as

$$P(C) = \int d\mu \mathcal{P}(C|\mu)P(\mu), \quad P(\mu) = \int \delta(\mu - S_\nu At)P(S_\nu)dS_\nu = \left. \frac{P(S_\nu)}{At} \right|_{S_\nu=\mu/At}. \quad (3.3)$$

In this prescription, we first compute the distribution $P(\mu)$ of the mean number of counts, and assume these counts are the result of a Poisson process (completely uncorrelated) to obtain $P(C)$.

Assuming independence between multiple energy bins, we can merge bins by convolving the distributions in each bin. Indeed, the total integrated flux S_ν over a collection of bins is equal to the sum of the integrated fluxes in each bin. This extensive property of integrated fluxes/counts is useful to account for the fact that the effective area A is energy-dependent: we can generate $P(C)$ in some large number of narrow energy sub-bins, where the effective area varies across sub-bins but remains constant inside each one, and then we can convolve the $P(C)$ ’s to merge the sub-bins into a single bin. We refer the interested reader to Appendix A for further discussion of this construction.

As a tradeoff between wanting to exploit the spectrum and hoping to circumvent the low statistics inherent in this endeavour, we generate $P(C)$ in three final energy bins, with edges at [25, 100, 1000, 5000] TeV. In the real data, there are 34 events in the 20-100 TeV bin, with a relative Poisson noise of $\sqrt{34}/34 \sim 17\%$ only marginally larger than that of the full dataset ($\sqrt{53}/53 \sim 15\%$). Of the remaining 19 events, only 3 events lie in the 1-5 PeV bin [4].

Since we are working with relatively wide energy bins, we assume for simplicity that the deposited energy and the neutrino energy are equal, even though this is a poor approximation

for tracks. We also neglect uncertainties due to the energy resolution (cf. Sec. 6.1). These are $\sim 5\%$ and $\sim 15\%$ systematic and statistical effects, respectively [77]. Our treatment of the anisotropy of the exposure and its dependence on the incident flavour ratio are discussed in Appendices A.2 and A.3.

3.3.2 Discussion

The count distributions $P(C)$ for our extragalactic sources are, in first approximation, Poisson distributions with means determined by the “diffuse peak” of $P(F)$, and the energy/declination-dependent effective area in that pixel. Given the significant tail of $P(F)$, the distribution has a skew, such that the location of the peak and the location of the mean do not coincide. When we observe the sky, our observation of event counts is biased by this skewness, as we are more likely to observe the most probable number of counts than the mean number. As discussed above, this bias is increasingly prominent as the pixel size decreases or as the unresolved sources become rarer.

The skewness-induced reduction in the anticipated number of counts is automatically accounted for by using the full $P(C)$ of Eqn. (3.3) rather than the average $\langle C \rangle$ of source populations. However, amongst other things, this weakens upper limits determined from the population-average contributions of these sources to the diffuse flux. Such a weakening of upper limits derived using averages has already been discussed in the context of dark matter constraints from the diffuse gamma-ray background [46].

Because SFGs are so abundant, this bias is at the percent level for these sources: the average-derived limits on SFG contributions of, e.g., Ref. [44] are only a few percent weaker than the limits one would derive using the full distribution — but the fact that such studies of SFGs do not suffer from this bias could not have been known without using their $P(F)$.

For 2FHL sources, on the other hand, the mean and mode of $P(F)$ differ by factors of 0.4 in showers and 6.7 in tracks, significantly reducing their anticipated count yield despite not affecting their mean count yield. Knowledge of the total distribution $P(F)$ is, however, not necessary to get a good approximation when sources are sufficiently rare that $P(F) \approx P_1(F)$. For example, Ref. [62] uses the blazar source count distribution $dN/dF \propto P_1(F)$ to derive its limits which (as a consequence of $\langle N' \rangle = 0.42$) is a good approximation to the full $P(F)$ in tracks: the 20% upper limit on the blazar contribution derived therein is not affected by this skewness. Note however that the stacking procedure in Ref. [62] increases the effective $\langle N' \rangle$ in the stacked pixel and thereby deteriorates the quality of this approximation, see also our discussion in Sec. 5.1.2.

Correcting for the skewness-induced bias just discussed using Eqn. (3.3), the average number of counts $\langle C \rangle = \sum_C C P(C)$, cumulative over all energies and declinations, in both tracks and showers, is then 2.2 events for SFGs and 3.3 events for 2FHL sources. Notice, in the hard-spectrum blazar case, that this is approximately equal to the number of events for 1–5 PeV in the HESE data [4]. Even after subtracting the 28 atmospheric events predicted by our atmospheric model from the 53 actually observed, one expects roughly 20 of these events to remain unexplained by our fiducial model. Hence, the expected contributions from SFG and from 2FHL models are each about 10–15% of the astrophysical flux, well below known upper limits [26, 44, 62]. The statistical significance with which we can say our data-driven model is incomplete (amongst other things we can learn from one-point functions) will be investigated in the next sections.

4 Analysis (I): Methodology

To show that our systematic conceptual approach is very general, we present in this study three different one-point analyses: a point source detection analysis, a probable clustering analysis, and a likelihood analysis based on the count distributions of individual pixels.

4.1 Resolvability of point sources

Let us consider the ideal limit of a telescope with fixed angular resolution but infinite exposure. The Poisson noise in such an instrument would be negligible, it would effectively be sensitive to $P(F)$ directly rather than $P(C)$. Even in this idealised situation, the finite angular size of a pixel means that not all sources can be individually resolved: the diffuse peak due to unresolved sources of a given population is an intrinsic background to point sources of the same population. In what follows, we argue that even an ideal detector with the IceCube angular resolution would be extremely unlikely to detect SFGs as point sources.

A point source is basically just a localised flux observed in excess of a predetermined threshold value F^{pt} . The probability that such a localised excess can be found in any single pixel is given by the exceedance (complementary cumulative) distribution of $P(F)$, and the typical number of excesses we expect to see in N_{pix} pixels is

$$N_{\text{pt}}(F^{\text{pt}}) = N_{\text{pix}} \int_{F^{\text{pt}}}^{+\infty} P(F) dF \approx N_{\text{pix}} \frac{N(F > F^{\text{pt}})}{N_{\text{MC}}}, \quad (4.1)$$

where the latter has been obtained by estimating the exceedance probability by Monte-Carlo sampling from $P(F)$. We recall that $N_{\text{pix}} = 48$ for showers and $N_{\text{pix}} \sim 5 \times 10^4$ for tracks. The fluctuations around the expected number of sources are assumed to be Poissonian.

An analytic approximation to the exceedance probability, valid in the high flux power-law tail where a single source dominates the flux in the pixel, was derived in Ref. [46]. When this approximation matches the Monte-Carlo estimation above, we can be relatively confident that the localised excesses correspond to single astrophysical objects. However, there is a region between the diffuse peak and the power-law tail where multiple bright sources jointly contribute to the flux and might be confused for a single point source. Because of this possible confusion, the number of localised excesses is always greater than the number of astrophysical point sources. The upper limits for the detection of astrophysical sources we will determine using localised excesses are therefore conservative. Also note that stacked searches [43, 62] are intrinsically looking for localised statistical excesses rather than individual point sources.

In order to study excesses above the diffuse background, we must characterise the Gaussian peak of $P(F)$. To do this, we take the samples drawn from $P(F)$, and censor the values above the peak of the distribution where non-Gaussianities due to the power-law nature of the single-source distributions might arise. We then fit the samples below the peak to a doubly truncated normal distribution using the maximum likelihood estimators derived in Ref. [78].⁴ The estimated mean $\hat{\mu}$ and standard deviation $\hat{\sigma}$ of the diffuse peak of each population (reported in Table 1) can then be used to define flux thresholds of localised excesses above the diffuse peak with various signal-to-noise ratios, $F^{\text{pt}}(\text{SNR}) = \hat{\mu} + (\text{SNR})\hat{\sigma}$.

⁴Our truncation points are (i) the flux at which the distribution peaks, and (ii) a flux of $F = 0$. We still determine $\hat{\mu}$ from the Monte Carlo samples for the sake of self-consistency, in case the truncation point (derived from an interpolation of the samples) is not exactly at the distribution peak. See Sec. 6 for a discussion of effects that contribute to producing a non-Gaussian diffuse peak.

Using the complementary cumulative distribution of $P(F)$, these thresholds can be converted into the exceedance probabilities associated to any given signal-to-noise ratio SNR. These are larger than for a pure Gaussian because $P(F)$ is skewed. Indeed the rarer a given population of sources, the more skewed its $P(F)$ is (cf. Sec. 3.2) and therefore the more probable its exceedances are to have high signal-to-noise ratio.

In order to see such a source from a rare population, however, it must also be brighter than the diffuse backgrounds of all other source populations combined. Treating these $P(F)$ peaks as Gaussians comes with the benefit that the diffuse backgrounds due to multiple populations can easily be convolved into a single diffuse and isotropic extragalactic neutrino background with mean intensity $\sum_i \hat{\mu}_i$ and width $\sqrt{\sum_i (\hat{\sigma}_i)^2}$. Similar thresholds $F_{\text{pt}}(\text{SNR})$ may be defined for this total background, and the exceedances of individual populations above this total background may be forecasted (cf. Sec. 5.1).

Heuristically, the skewness of $P(F)$ is due to barely-resolvable point sources in this infinite-exposure idealisation. Notice that decreasing the pixel size increases the skewness of $P(F)$ (cf. Fig. 3), and so increases the typical signal-to-noise of excesses: barely-resolvable sources (e.g. the “hot spots” of flux maps [5, 79]) may become resolvable to future instruments. By extension, the excess skewness of $P(C)$, over the skewness of a Poisson distribution in IceCube, is related to the possible improvement in discovery potential of future point-source searches in an instrument with improved angular resolution, such as KM3NeT (ARCA) [80] or IceCube-Gen2 [81].

4.2 A “Pointless” clustering analysis

The IceCube collaboration has found no evidence for clustering by looking for hot spots consistent with point sources [4, 5]. But resolving point sources is not the only way we might see clusters of events: in a detector with realistic exposure we can also exploit the statistical properties of localised event clusters due to multiple bright but unresolved sources or even shot noise fluctuations.

Given a fixed pixel size, the one-point function is the most straightforward tool to study neutrino clustering. Indeed, we can directly consider the “average number of clustered neutrinos per pixel” or the “rarity of a cluster of $N \geq 2$ or more events,”

$$\langle C \geq 2 \rangle = \sum_{C=2}^{\infty} CP(C), \quad \mathfrak{c}(N) = \sum_{C=N}^{\infty} P(C). \quad (4.2)$$

In the ideal case that the data reproduce exactly a Poisson distribution with a mean μ , it is easy to show, e.g., that $\langle C \geq 2 \rangle = \mu(1 - e^{-\mu})$. However, not only the naïve analysis above would not account for the different angular resolution of tracks and showers and the anisotropic exposure, it would also eschew distributional information by using a single μ value rather than the full $P(\mu)$ from Eqn. (3.3). One should expect two effects to emerge from the power-law tails of astrophysical contributions: on the one hand, this tail increases the number of clustered events; on the other hand, this tail contributes a skewness that pushes the most likely values of the distribution to lower flux, as part of a distribution with a fixed mean, resulting (after marginalisation) in less event clustering overall [46].

To go beyond the mean values, let us consider the following per-pixel (p) clustering statistic with a model-dependence \mathbf{M} on the flux distributions and the detector response from Sec. 3:

$$\mathfrak{c}^{(p)} = \begin{cases} \sum_{C=d^{(p)}}^{\infty} P(C|\mathbf{M}) & \text{if } d^{(p)} \geq 2 \\ 1 & \text{otherwise} \end{cases}. \quad (4.3)$$

The total amount of clustering associated to a dataset $\{\forall p, d^{(p)}\}$ is then quantified by $\mathfrak{C} = \prod_p \mathfrak{C}^{(p)}$, and data sets with more clustering (given the same $P(C|\mathbf{M})$) will have a larger $-\ln \mathfrak{C}$. Since we care only about directional information in this test statistic, we need to treat coincident neutrinos of different energies as members of the same cluster. To do so, we follow the prescription of Sec. 3.3.1 and Appendix A and convolve the count distributions of different energy bins to produce the $P(C)$ of Eqn. (4.3). The same logic applies to coincident tracks and showers: accurate track pixels were first coarse-grained into shower-sized pixels (cf. Appendix A.2), and then convolved with the shower pixel covering the same patch of sky.

A clustering analysis using \mathfrak{C} is in a sense a generalisation of the multiplet method applied to the IceCube data in Ref. [43]. In their analysis, the average number of sources producing $C \geq 2$ tracks was computed from populations of “effective standard candles,” i.e., populations with a luminosity density $L_{\nu\mu}^{\text{eff}}$ fixed to an effective value (as a proxy for the full luminosity function). In our distributional study, the average number of sources producing $C \geq k$ track or shower events could easily be computed by convolving the detector response (cf. Sec. 3.3.1) over the single-source distributions of Sec. 2; but this quantity would not fully exploit the clustering statistics when multiple sources are present in the same pixel, which are automatically included in the test statistic \mathfrak{C} .⁵

4.3 Single-pixel Likelihood Analysis

The quantity that we have computed to be compared to the data is the anisotropic and spectral probability distribution of event counts. Since there are very few events in our dataset, a χ^2 analysis of count histograms would be untrustworthy. Here, we opt to work directly with the likelihood of the data. The likelihood per pixel (\mathcal{L}_p) is a function of the number of counts in a given pixel p and in a given energy range ΔE_ν [50]. Therefore, the total (binned and marginalised) likelihood of a one-point analysis is:

$$\mathcal{L} = \prod_s^{\text{signal}} \prod_{\Delta E_\nu}^{\text{energy bin}} \prod_p^{\text{pixel}} P(C = d^{(s, \Delta E_\nu, p)} | \mathbf{M}), \quad (4.4)$$

under the assumption that all the count data $d^{(s, \Delta E_\nu, p)}$ in each of the pixels, energy bins, and signal types/topologies are mutually independent. If detectors other than IceCube were considered in this analysis, an additional product over independent instruments could also be considered (cf. Appendix B). In order to justify the assumption that signal topologies are independent, we explicitly do not consider the “coincident” event (#32) in this analysis.

The likelihood Eqn. (4.4) allows us to assess the predictive power of a model. Indeed, we can draw from $P(C|\mathbf{M})$ to generate mock data and the exact distribution of the test statistic $TS = -2 \ln(\mathcal{L})$ under the null \mathbf{M} , from which a poorness-of-fit for the likelihood of the real data may be computed as a p -value (cf. Sec. 4.4). All the isotropic components in this study (atmospheric foregrounds, SB and SF-AGN (SB), and 2FHL) contribute to \mathbf{M} . One feature of this likelihood is that empty pixels (non-observations) also carry information, and that this information is statistically exploited as we will discuss in the next paragraphs. In addition to tracks and showers, IceCube is in principle sensitive to a number of ν_τ -specific topologies [82]. Events in these signal channels would almost certainly be of astrophysical origin, and the

⁵The number of sources contributing k events is the quantity estimated in one-point fitting studies, which use probability-generating functions to disentangle numbers of clusters into numbers of sources.

nondetection of these topologies can set strong upper limits on the astrophysical ν_τ flux [83]. However, these unobserved topologies were not considered in our model of the IceCube flavour response (cf. Appendix A.3) and do not contribute to \mathcal{L} .

By using $P(C|\mathbf{M})$ in the likelihood rather than just a Poisson at the mean of $P(F)$, we automatically account for the skewness-induced difference between the peak and mean values of the flux discussed in Sec. 3.2.2. However, this skewness drives our prediction to lower counts, and an interesting effect occurs when both of the following occur:

1. \mathbf{M} produces a count distribution per pixel of the form

$$P(C) : \{P(0) \approx 1 - \epsilon ; P(1) \approx \epsilon ; \text{rest} \approx 0\} , \quad (4.5)$$

2. \mathbf{M} is mis-specified, and produces a larger total number of counts than in the real data.

The effect of this convergence of features is that the real data can (counterintuitively) give a smaller $-2 \ln \mathcal{L}$ than any of the mock data generated from \mathbf{M} itself. This effect can then be used as a diagnostic for models that overpredict the number of counts. In the context of a one-point fluctuation analysis, this could mean either overpredicting the peak number of counts or overpredicting the amount of clustering (e.g., due to an excess of unresolved point sources in the model).

4.4 Digression on p -values

We conclude our methodological overview with a few cautionary words about statistical significances [84]: the distributions of the test statistics employed are non-parametric, and we find empirically that they are asymmetric. Therefore we follow the prescription in Ref. [85] and report the one-sided p -value along with the direction it deviates from the bulk of the distribution of the test statistic. Although we do so at times out of convenience to the reader, we recommend against converting these directed- p -values into Gaussian σ 's. In fact ignoring the p -value from the other tail would artificially inflate this significance and estimating it is error-prone [85]. This is particularly true for the lower ‘‘tail’’ of our clustering statistic \mathfrak{C} (cf. Fig. 5), for which no such p -value exists.

After generating mock datasets for each model, we partition the mock datasets into five subsets to generate the sample mean and standard errors of the p statistic subject to the limited number. Any p -values that are too small to resolve within reasonable computational time are then quoted as upper limits. Since the uncertainties on p are due to finite number of mock datasets rather than to interesting physics, they are not systematically reported.

In order to extract as much information as possible, our analyses of the HESE data will typically focus on subsets of these data. The global significance of independent p -values can be computed by correcting for the look-elsewhere effect with trial factors. Alternatively, these p -values may be combined with meta-analysis techniques. Because the difference between, e.g., 2.7σ and 2.8σ is somewhat irrelevant to our mock-data-limited and systematics-prone discussions (see above and Sec. 6), we consider it is sufficient to correct our p -values with Bonferroni trial factors (i.e., we multiply significances by the number of trials to estimate the post-trial significance), and we combine p -values testing the same hypothesis on different data subsets with Fisher’s method $-2 \sum_i^k \ln(p_i) \sim \chi_{2k}^2$. Since the test statistics in this study are built from the marginal likelihood $P(C|\mathbf{M})$, they have no explicit dependences on unknown parameters and there is essentially no distinction between Fisherian (‘classical’) and Bayesian (‘predictive’) p -values.

5 Analysis (II): Results

In this section, we apply the statistical tools introduced in the previous sections. We discuss upper limits on the resolvability of blazars and SFGs in IceCube, and we perform various model-based one-point probability distribution analyses.

We have seen in Sec. 3.3.2 that our astrophysical+atmospheric models produce $\mathcal{O}(20)$ neutrinos less than the HESE data. Given the limited neutrino dataset to which we’re comparing the model, and all the caveats to be specified in Sec. 6, we invite the reader to think of the following exploratory analyses first and foremost as proofs of concept for the methods.

5.1 Detectability of star-forming galaxies and blazars as point sources

The diffuse backgrounds of unresolved sources are an intrinsic and inescapable feature of any abundant astrophysical population observed with low angular resolution, but population self-backgrounds are not the end of the story. Indeed, sources visible over the *total* astrophysical diffuse flux need to be far brighter and, because flux distribution tails are power-law-like, such bright sources are typically rather rare.

Since the angular resolution is the determining factor in this self-background effect, the number of sources we expect to resolve depends on this angular resolution. Our discussion of each source class’ resolvability prospects needs to address tracks and showers separately. In this forecast we focus on spectral intensities at $E_\nu = 100$ TeV, in order to evade the atmospheric backgrounds more prominent at lower energies, while maintaining a reasonable SFG contribution (spectrum of $\Gamma = 2.2$) relative to the blazar contribution (spectrum of $1 - s \approx 0.65$). The diffuse contributions of the components are summarized in Table 1.

Table 1: Parameters of the diffuse astrophysical neutrino flux peaks at 100 TeV, in showers and in tracks and in units of $10^{-20} \text{ cm}^{-2} \text{ s}^{-1} \text{ sr}^{-1} \text{ GeV}^{-1}$. Note that the mean contribution $\hat{\mu}$ in each population is slightly larger for showers than tracks, while the standard deviation $\hat{\sigma}$ in tracks is wider than showers, as discussed in Sec. 3. The 3σ and 5σ self-background exceedance probabilities per pixel for each subpopulation are also reported.

100 TeV	Showers ($\theta \sim 30^\circ, N_{\text{pix}} = 48$)			
Population	$\hat{\mu}$	$\hat{\sigma}$	$> 3\sigma$	$> 5\sigma$
2FHL	2.60	0.206	43%	32%
SF-AGN (SB)	10.61	0.024	10%	1.5%
SB	6.40	0.016	6.7%	1.1%
(All)	19.6	0.25		
100 TeV	Tracks ($\theta \sim 1^\circ, N_{\text{pix}} \sim 5 \times 10^4$)			
Population	$\hat{\mu}$	$\hat{\sigma}$	$> 3\sigma$	$> 5\sigma$
SF-AGN (SB)	10.33	0.84	2.5%	0.25%
SB	6.15	0.48	4%	0.4%
(All)	16.48	0.97		

5.1.1 Star-forming galaxies

The expected number of SFG localised excesses resolvable above the diffuse background at 100 TeV, by a detector with an infinite exposure and with the IceCube angular resolution for tracks are illustrated in Fig 4. In the real data these point sources must also be extracted from the background of other (unmodeled) extragalactic contributions, and the atmospheric foregrounds, which in our model shine an order of magnitude brighter than all SFGs combined at 100 TeV. The number of such localised excesses is $N_{\text{pt}} = 17.8 \pm 4.2$ for SF-AGN (SB) and $N_{\text{pt}} = 4.9 \pm 2.2$ for SB for a 3σ threshold. The fact that we forecast resolving more SF-AGN (SB) than SB is related to the locations of the $P(F)$ distributions (cf. Sec. 3.2.2), or more precisely, the locations of the tails of these distributions. In Fig. 3 we see that, above intensities of about $-18.75 \text{ dex cm}^{-2} \text{ s}^{-1} \text{ sr}^{-1} \text{ GeV}^{-1}$, the SF-AGN (SB) tail dominates over the SB tail, and so if there are any such bright sources at all, they are more likely to be from the SF-SGN (SB) subpopulation.

In showers, the expected number of SFG excesses over the SFG+2FHL background is essentially negligible given the order-of-magnitude difference between the estimated standard deviations of the diffuse backgrounds in Table 1. A Monte-Carlo estimate suggests that we might see $N_{\text{pt}} \sim 10^{-2}$ excesses with a negligible significance of $10^{-4}\sigma$ due to SF-AGN (SB); and no excesses due to SB, which have both a smaller $\hat{\mu}$ and a smaller $\hat{\sigma}$. We conclude that SFGs are an intrinsically diffuse background with 30° pixels, even with an infinite exposure.

These non-detectability claims are energy and model dependent, but finite detector exposures and discrete neutrino events would further deteriorate the point-source detection prospects. The number of plausible associations with SFGs [86, 87] is bounded from above: we should not expect any corroboration of claimed associations with future data. The SFG non-detectability in IceCube should be expected also from similar studies in gamma-rays: A one-point-fluctuation study of Monte-Carlo simulations of unresolved blazars and SFGs in *Fermi* (which has an angular resolution comparable to that of IceCube tracks) finds that blazars are fitted by a diffuse unresolved point source template, while SFGs are absorbed into a diffuse isotropic template [51].

In short, our model makes two predictions for SFGs due to self-backgrounds effects: firstly, SFGs constitute a diffuse background in showers; secondly, the detectability for SFGs in tracks is still very poor. We might see $N_{\text{pt}} \sim \mathcal{O}(25)$ out of the $N_{\text{tot}} \sim \mathcal{O}(10^8)$ sources predicted from *Herschel* SB and SF-AGN (SB) luminosity functions, and this prediction needs to be further tempered by unaccounted-for extraterrestrial and atmospheric backgrounds and the finite IceCube exposure, especially at energies different from 100 TeV.

In the light of these results, we draw attention to the SFG cross-correlation programme pursued in the literature [17, 86, 88]. We have quantitatively shown that SFGs are most probably incapable of acting as localised excesses in IceCube, even if access to far more data than currently available were possible. A cross-correlation of IceCube data with SFG catalogues, which relies on such excesses, is essentially guaranteed to produce a null result (except when a significant correlation is spuriously driven by fluctuations or non-SFG contaminations). This is consistent with the null [5, 17, 52] or statistically insignificant ($p \sim 0.3\text{--}0.5$ post-trials [88]) results obtained when attempting to correlate these high-energy events with SFGs.

Since our prediction of a null result is a function of the number of SFGs per pixel, the only way around such negative predictions is to wait for large quantities of data from a neutrino telescope with an angular resolution significantly better than the $\sim 1^\circ$ achieved in

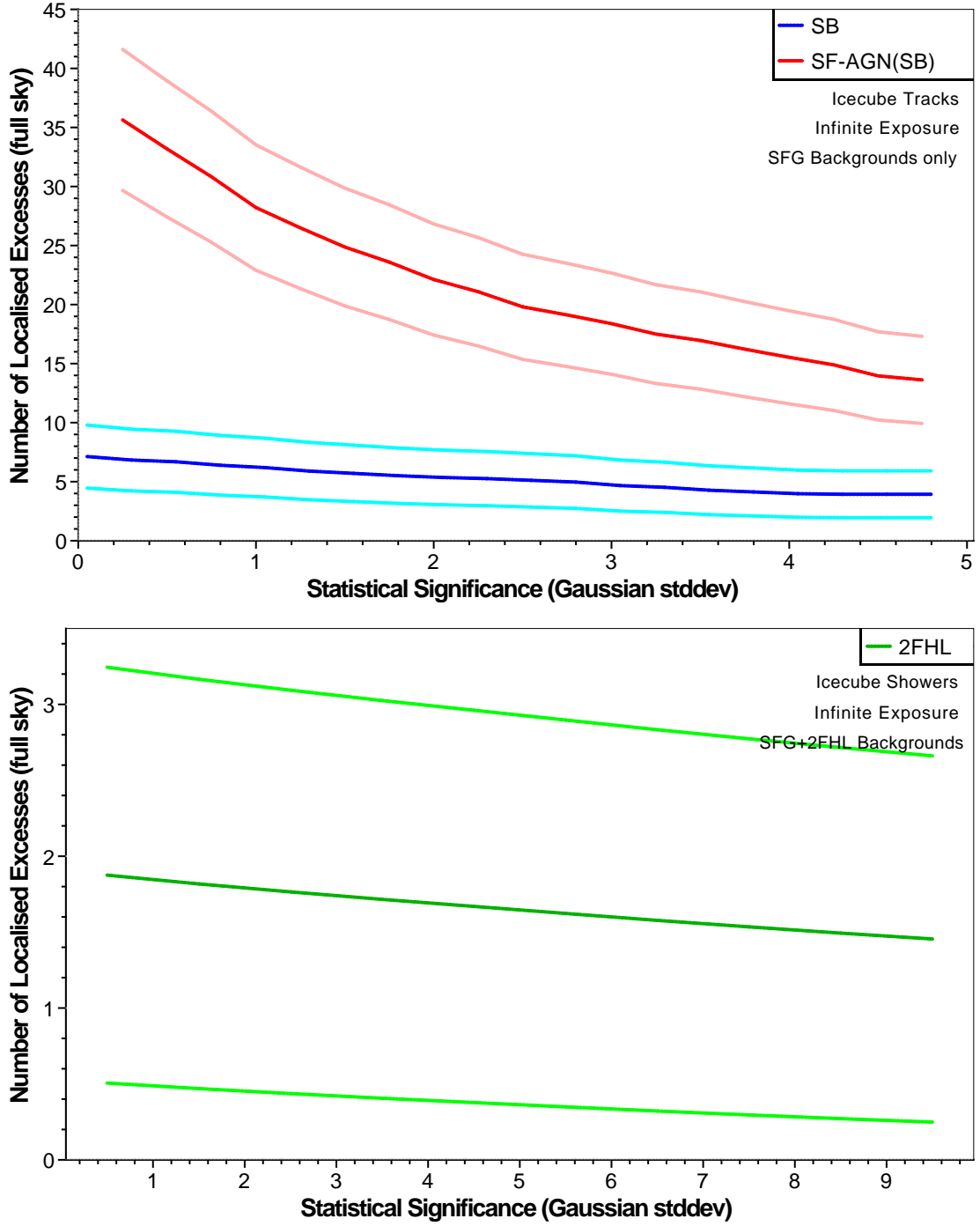


Figure 4: *Top:* Point-source detection prospects (N_{pt} vs SNR) for SB (blue) and SF-AGN (SB) (red) in 100 TeV tracks assuming infinite exposure, IceCube angular resolution, and no backgrounds other than the self-background from SFGs themselves. Poisson (1σ) error bands on N_{pt} are given. These detection prospects are thus intrinsic and conservative upper limits. *Bottom:* Detection prospect upper limit for 2FHL in 100 TeV showers, assuming backgrounds from 2FHL and SFG.

IceCube tracks.⁶ Sub-degree angular resolutions for tracks, as expected, e.g., for IceCube-Gen2 [81] and KM3NeT (ARCA) [80], may allow the nearest SFG point sources to be detected [87]. However, the Galactic foregrounds for such a detection in ARCA will be significant. Note also that stacking the pixels of prospective SFG sources (as discussed in Ref. [43]) increases the effective pixel size, exacerbating this self-background effect (as discussed for blazars above).

5.1.2 Blazars

As discussed in Sec. 3, essentially none of the 2FHL sources contribute to their own diffuse background in tracks: all of the modeled 2FHL sources are resolvable as localised excesses in our infinite-exposure, high-resolution detector. This does not, however, mean that they can all be resolved as individual objects given the backgrounds and shot noise in IceCube. Also, this does not even guarantee a statistical detection of these sources. Indeed, when stacking the $1^\circ \times 1^\circ$ muon tracks of ~ 900 potential blazar sources in the 2LAC catalogue [62], the effective pixel size is similar to that of a $30^\circ \times 30^\circ$ shower, and so the effective $P(F)$ of the stack resembles that of a single shower pixel, the self-background effect becoming relevant again.

In showers, the blazar self-background effect does matter: at 100 TeV, only 32% of the 2FHL sources can be resolved at 5σ , even before accounting for other backgrounds. In our model of the astrophysical diffuse flux due to the combination of diffuse fluxes from SB, SF-AGN (SB), and 2FHL sources, we only expect on average $N_{\text{pt}} \sim 1.8 \pm 1.3$ excesses above the total diffuse extragalactic background at 100 TeV (Fig. 4 suggests this upper limit on N_{pt} is relatively independent on the detection significance).

Although this model does not necessarily rule out associations between single high-energy showers and individual blazars [20, 28, 65, 89], it does place a strong (albeit model-dependent) upper limit on the number of blazar associations we should expect to corroborate by accumulating more shower data in a finite instrument such as IceCube. This upper limit could be further strengthened by accounting for other subpopulations not considered in our model. At energies below or above 100 TeV, this upper limit in IceCube would be dominated by the atmospheric backgrounds or shot noise respectively.

5.2 Clustering analysis

Applying Eqn. (4.3) to the 53 observed high energy events,⁷ we find $-\ln \mathfrak{C} = 47.4$ over the full sky. Applying \mathfrak{C} to mock data generated from $P(C|\mathbf{M})$ then generates the distribution of this test statistic under the null hypothesis, shown in Fig. 5. We easily see that the model produces far less neutrino clustering than observed (typically $-\ln \mathfrak{C} \lesssim 30$).

This is *not* a detection of significant clustering in the data, fully consistent with the null results in anisotropy searches [7–9]. This is due to the fact that our model underpredicts the data by about 20 counts (cf. Sec. 3.3.2), and with less counts per pixel overall one should also expect less random clustering of these counts to occur. Although we are presumably recovering a discrepancy we already knew about, notice that we are indeed exploiting the clustering properties of the Poisson shot noise of isotropic components to see it.

⁶Note that the point-source detection prospects forecasted in [87], in which psf-smoothed samples of $P_1(C) \sim \delta(C - L_{\text{eff}}(z)n_s \times \text{constant exposure})$ for a single population of sources describing all cosmic ray accelerators were used to approximate samples of $P(C)$, illustrate (qualitatively) how self-backgrounds decrease with the angular resolution also in detectors with finite exposure.

⁷The coincident event (#32) has no directional information and was not used in this analysis.

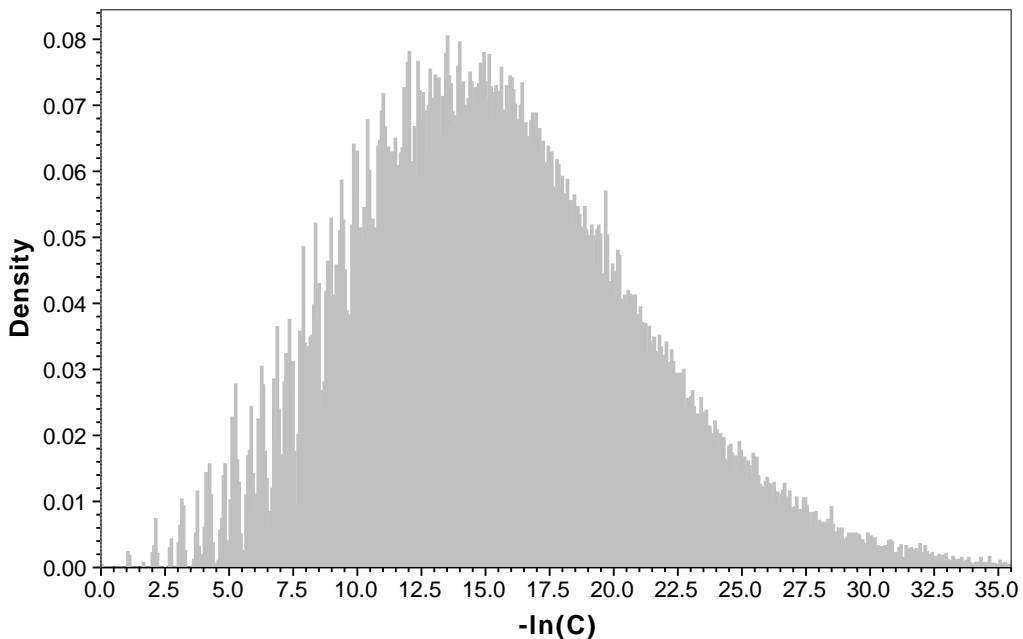


Figure 5: Null distribution for $-\ln \mathfrak{C}$ applied to full-sky mock datasets drawn from our model (including atmospheric foregrounds, unresolved SFG and 2FHL point sources, and anisotropic energy-dependent exposure). The regular, discrete peaks (most prominent at “low clustering”) are due to the finite combinatorics behind producing small amounts of clustering in a finite number of 30° pixels. The value observed in the IceCube data is $-\ln \mathfrak{C} = 47.4$.

Since $\mathfrak{C} = \prod_p \mathfrak{C}^{(p)}$ is separable, this clustering analysis can be performed on small patches of the sky. We study the southern and northern hemispheres ($\delta \lesssim -20^\circ$, and symmetrically in the north), plus an equatorial band ($-20^\circ \lesssim \delta \lesssim 20^\circ$), where IceCube effective area is maximised, to study whether the observed clustering is consistent with that predicted by our model. We then have $-\ln \mathfrak{C}^{(N,E,S)} = (13.7, 2.0, 31.6)$, with three trials to account for in our look-elsewhere corrections. In the north, we find that the typical $-\ln \mathfrak{C}$ is smaller in the mock data than in the real data, i.e., less clustering in the mock than in the real data, but with a small one-sided $p = 0.12$ ($\sim 0.7\sigma$ pretrials). At the equator, we find more clustering in the mock data than in the real ones, but again with a negligible one-sided $p = 0.24$ (pretrials).⁸

There is more clustering in the southern hemisphere of the real IceCube data than our model could predict: our knowledge of the significance is in this case limited by the number of Monte-Carlo realisations to the upper bound $p < 3 \times 10^{-7}$ (one-sided, post-trials). This is roughly equivalent to a 4.9σ lower limit on the significance. This discrepancy between the discrepancies in the north and in the south is *not* an observation of astrophysical anisotropy, fully consistent with null results of anisotropy searches [7–9]. Indeed, IceCube has a higher exposure in the northern hemisphere, so we expect a larger number of counts there than in the south. We also expect that with the larger Poisson errors associated to this larger

⁸The limited number of distinct mock datasets we can generate with eight pixels in the equatorial declination band discretises the support for the distribution of $\mathfrak{C}^{(E)}$. This in turn generates the bin-height alternation in the full-sky distribution of Fig. 5, particularly prominent in the left-hand tail.

number of counts, the north is more tolerant of model mis-specifications than the south (even though all the contributions to this flux are isotropic). This interpretation is consistent with the even less significant p -value in the equatorial band, where the exposure is maximised and Poisson errors are largest.

The combined significance of these three discrepancies (according to Fisher’s Method) is equivalent to 4.9σ : our data-driven model of the IceCube flux (containing only atmospheric, SFGs, and blazars) is rejected for having less clustering than the HESE data, which is known to be consistent with isotropy. In order to accurately predict the data, one must either fine-tune the model to fit the data (by revising our extrapolations from the *Herschel* and *Fermi* data) or add additional components to the model. Since the model is still missing sources one would expect to contribute to the flux (e.g., cf. Refs. [10, 27, 30]), we believe it is premature to attempt the former (see also Sec. 6.3). Updates to the model are left to future work.

5.3 One-point fluctuation analysis

From Sec. 3.3.2 and the clustering analysis above, we know that the model does not produce enough neutrino event counts (~ 33) to explain the data ($= 53$). But since the global likelihood (Eqn. (4.4)) is a product of independent single-datum-likelihoods, we can decompose the contributions of subsets of the data to our $-2\ln(\mathcal{L})$, to further diagnose our model.

5.3.1 Results

We will study three energy bins with edges at [25, 100, 1000, 5000] TeV (cf. Sec. 3.3.1), separately in the north and south hemispheres to fully exploit the anisotropy of the exposure. We signal-optimize away the data in the equatorial band which, as we have seen above, is least sensitive to model mis-specification. We will also decompose the likelihoods into the separate contributions from tracks and showers; however there are not enough shower data in the northern hemisphere above 100 TeV to perform this analysis. Counting these subdivisions of the data shows there are ten trials to account for when computing global significances.

The track prediction is dominated by conventional atmospheric neutrinos and veto-passing muons, and is surprisingly satisfactory given how crudely we modelled the atmospheric neutrino contribution. In the south we obtain one-sided p -values greater than 0.3 pre-trials, suggesting no discrepancy between the model and the data. In the north, the model remains mostly consistent with the data, with a $p = 0.08$ deficit below 100 TeV, a $p = 0.32$ excess at intermediate energies, and a $p = 0.15$ deficit above 1 PeV (all pre-trials). The combined significance of these six p -values is 1σ according to Fisher’s method. This suggests that our un-fine-tuned model can predict the track data fairly well, though improving the atmospheric foreground models in an attempt to extract astrophysical information out of tracks is beyond the scope of this preliminary analysis. In what follows, only the shower data are studied to extract astrophysical information, but tracks remain useful to the extent that they corroborate that the detector modeling and atmospheric models are correct.

The results of a likelihood analysis of shower-data are summarised in Table 2. The direction of the discrepancies encoded by these p -values confirm that we are (significantly) underpredicting the counts. At low energies, as discussed in Sec. 5.2, the apparent anisotropy in the p -values is consistent with the difference in exposure between the north and the south, our method being most sensitive to mismodelling in the south. This discrepancy in southern showers below 100 TeV has a significance $\sim 3\sigma$ when accounting for the 10 trials.

At higher energies, the discrepancy between the model and the data is less severe. In the 100–1000 TeV range, the discrepancy is of a similar magnitude, 2.7σ (post-trials). At the

highest energies, the hard 2FHL component is the main contribution: it underpredicts the PeV data, but only with a marginal significance of $\sim 1.1\sigma$ (post-trials). Note that our SFG model does not have a spectral break at high energies [16]: fixing this model shortcoming would decrease the anticipated counts from the model, and increase the significance of the discrepancy. At high energies in the north, there are not enough events to perform the analysis.

5.3.2 Discussion

The one-point analysis can also be used to “characterise” the discrepancy (to a first approximation). Assuming that the analysis of tracks above has validated the detector and the atmospheric models, this discrepancy is deduced to be astrophysical. A further study of the energy-dependence of this discrepancy in the southern hemisphere (where our method is most sensitive to model mis-specifications) suggests that the unmodelled contribution is missing for 25–1000 TeV, but not above (cf. Table 2). It has a soft spectrum and/or a cutoff at high energies. We can even estimate the significance with which we need such an astrophysical component by combining the relevant p -values.

Combining the four p -values in Table 2 with Fisher’s method (i.e., neglecting the six trials in tracks, which we know to be atmospheric-dominated) yields a global significance equivalent to $\sim 4.8\sigma$. This is only marginally better than the evidence that our model’s expected number of showers ($\langle C \rangle \approx 19$) is underpredicting the data ($C = 39$ showers) simply using a χ^2 test, $(39 - 19)^2/19 \rightarrow 4.5\sigma$. The one-point analysis may not seem to add much over a standard model-based analysis, but there are a few subtleties worth mentioning here:

1. Our computation of $\langle C \rangle$ automatically accounts for the skewness-induced bias discussed in Sec. 3.2.2. However, this is not the case in analyses based on $\langle I_\nu \rangle$, where the one-point skewness is ignored. Now notice that, e.g., $(39 - 20)^2/20 \rightarrow 4.1\sigma$. All other things equal, one-point methods based on $P(I_\nu)$ are therefore statistically stronger than analyses based on $\langle I_\nu \rangle$, because they are intrinsically correct for this bias.
2. Even though we are fully exploiting $P(I_\nu)$ behind the Poisson shot noise, there is simply not much more information to exploit given the number of events in the HESE data. As more data becomes available, we will increasingly be able to probe the higher moments of $P(I_\nu)$, and the added statistical power of this methodology should become more apparent.
3. A likelihood approach allows us to study low-count subsets of the data where the χ^2 would be unreliable. But even then, there are currently not enough showers above

Table 2: Real/mock shower-data upper p -values (pre-trials) in the northern and southern skies and in various energy bands. The model includes atmospheric, SFG, and 2FHL contributions. The discrepancy between the mock and real data has a combined $\sim 4.8\sigma$ significance.

Energy (TeV)	north	south
25 – 100	0.218 ± 0.004	$(7.4 \pm 0.7) \times 10^{-5}$
100 – 1000	N/A	$(1.85 \pm 0.3) \times 10^{-4}$
1000 – 5000	N/A	0.146 ± 0.007

100 TeV in the northern hemisphere to sensibly perform this analysis. This signal region is where one anticipates the conventional atmospheric background to contribute the least, so this analysis’ potential sensitivity to a mismodelling of prompt atmospheric or astrophysical components is not fully represented in the 4.8σ combined significance.

For a contrast of our model-based approach to other one-point fluctuation techniques, see Appendix B.

In summary, our likelihood analysis reveals a $\sim 4.8\sigma$ discrepancy between the model prediction for IceCube showers and the HESE data, that is especially pronounced below PeV energies. This discrepancy is insignificant (combined 1σ) in tracks, suggesting it is of astrophysical (rather than atmospheric) origin in our model. The anisotropy of the discrepancy appears to be consistent with the statistical method’s sensitivity to the anisotropy of the instrumental exposure.

6 Analysis (III): Discussion of systematics

The results presented above are subject to a number of caveats and uncertainties, which we discuss in this section. These fall into two categories: methodological caveats, which might introduce systematic effects; and astrophysical uncertainties, which translate into systematic uncertainties in our models.

6.1 Methodological systematics

Inadequacies in methodology are particularly vicious, since the biases they produce cannot be rigorously quantified using the tools that produce them. In this section, we discuss the two main blind spots in the single-pixel analyses above.

Firstly, the effects of extended sources that could potentially affect our “single pixel” results [46] were not studied. The instrumental point-spread function is also a relevant quantity to consider [50], as it is the energy resolution or the difference between deposited and real energy [77], amongst others. Ideally, a one-point analysis would account for these reconstruction uncertainties at the level of the detector model, however this is far beyond the scope of this first analysis. All of these potential systematic effects are related to our binning of the data into energy bins ΔE and pixels $\Delta\Omega$, and need to be addressed by (ongoing) efforts to unbin the one-pixel functions we have been discussing into true one-point functions. This unbinning would also avoid pixelising the data with Healpix (cf. Sec. 3.1) when performing our clustering and likelihood analyses, freeing these analyses from pixelisation artefacts.⁹

Secondly, although pixel exposure is treated anisotropically, the incident flux distribution was assumed isotropic. This approximation may be sufficient for studies of unresolved extragalactic sources, but morphological, spectral, and distributional templates will be necessary in the future to consistently account for atmospheric and Galactic contributions. Even for unresolved extragalactic sources, the assumption of isotropy may be too strong, as these sources are only *statistically* isotropic. The statistical clustering of unresolved sources is indeed known to affect the flux distributions, and in this study failing to account for this effect underestimates the non-Gaussianity of the flux distribution [75, 76].

⁹To check that this did not influence our results, we resampled the HESE showers within their angular uncertainties 1000 times and recomputed the clustering test statistic \mathfrak{C} of Sec. 4.2 and the log-likelihood $-2\ln\mathcal{L}$ of Sec. 4.3. These fluctuations do not significantly weaken these results.

6.2 Marginalisation systematics

In addition to the methodological systematics discussed above, we rely (for simplicity's sake) on the best-fit values of a number of uncertain parameters. This results in a likelihood that is partially profiled and partially marginalised, and this may introduce systematics. The flux models we have adopted for the SFG and the blazars depend on data-driven parameters that remain somewhat uncertain, and using only their best-fit values is clearly dangerous when extrapolating power laws. For example, one might naively expect the $\sim 20\%$ systematic uncertainty in the conversion $L_\gamma(L_{\text{IR}})$ (cf. Sec. 2.1.1) to shift the entire SFG distribution $P(F_\nu)$ in Fig. 3, but if this uncertainty were marginalised away the distribution would also broaden while it shifts. A similar line of reasoning holds for the uncertainties of the luminosity function itself. There is a $\sim 15\%$ uncertainty on the normalisation of the infrared LF for the SB subpopulation [57], which does not affect the single-source $P_1(F_\nu)$ but does affect the multi-source $P(C)$. Even then, such $\sim 20\%$ effects on ≈ 2.2 events from SFG in IceCube (cf. Sec. 3.3.2) cannot close the ~ 20 event gap between the SFG model (driven by *Herschel* and *Fermi* data) and the HESE events, which would be inconsistent with upper limits on the SFG contribution anyway [44].

Another very relevant example of the mixture between statistical and systematic uncertainties in one-point methods is that the gamma-ray fluxes (and their distributions) were extrapolated to high energies using a single value of the spectral slope Γ per population, rather than extrapolated with a marginalisation over the intrinsic scatter in Γ observed in each population. The uncertainties on the gamma-ray spectrum Γ are expected to affect the analysis systematically: consider the spectral flux $F_\gamma = F_{\gamma,0}(E_\gamma/E_{\gamma,0})^{-\Gamma}$, with $P(F_{\gamma,0}|E_{\gamma,0})$ and $P(\Gamma)$ independent and each approximately Gaussian. It can then be shown that F is normal-log-normally distributed [90]. Thus, marginalisation over Γ generates additional skewness in $P(F_\gamma)$, which might be used in future studies as a tool for studying unresolved source distributions that would otherwise be treated as Gaussians (cf. Sec. 4.1). However, in this study, keeping Γ as a fixed parameter represents a systematic overestimate of the gamma-ray fluxes. It is easiest when estimating this systematic effect to ignore distributions and look only at averages. The mean flux of $P(F_\gamma|E_\gamma)$, assuming $\Gamma \sim \mathcal{G}(\langle\Gamma\rangle, \sigma_\Gamma^2)$, is

$$\langle F_\gamma \rangle = \langle F_{\gamma,0} \rangle \times \left(\frac{E_{\gamma,0}}{E_\gamma} \right)^{\langle\Gamma\rangle + \sigma_\Gamma^2/2}, \quad (6.1)$$

in terms of the mean $\langle F_{\gamma,0} \rangle$ of an arbitrary $P(F_{\gamma,0}|E_{\gamma,0})$. The spectrum in our unmarginalised analysis is therefore systematically harder than the average spectrum of the flux by a term of order $\Delta\Gamma \sim \sigma_\Gamma^2$. As a consequence, the predicted contributions of our extragalactic components (extrapolated from GeV to the TeV–PeV energies) may be slightly overestimated. This may be particularly relevant for our phenomenological model of 2FHL sources, where the mixture of source populations yields an intrinsic spread σ_Γ of Γ that compounds our choice of a harder-than-anticipated average spectrum of $\langle\Gamma\rangle = 2.5$ in Sec. 2.2. Note that the observed spectral index uncertainty of 2FHL increases with the index itself, from $\Gamma = 2 \pm 0.5$ to $\Gamma = 5 \pm 2$ (partly because of the lower statistics) [59]. One might then roughly estimate the intrinsic $\sigma_\Gamma^2 \gg 0.5$. Accounting for this effect, or not choosing a harder-than-anticipated $\langle\Gamma\rangle$, would decrease the blazar neutrino flux of the model from Sec. 2.2. This would presumably increase the significance of the discrepancies encountered in the fluctuation and clustering analyses, and improve (hinder) point-source detection prospects for SFGs (blazars). However, since the Γ -marginalisation would also broaden $P(F_{\gamma/\nu})$ the net effect would come from more than just systematic shifts to the mean flux $\langle F_{\gamma/\nu} \rangle$.

6.3 Astrophysical model systematics

Our model adopts a simplified picture of the atmospheric foregrounds, and includes only two extragalactic source families. Both of these extragalactic models rely on extrapolations subject to astrophysical uncertainties (i.e., extrapolation of the neutrino spectra from the gamma-ray ones, the $L_{\text{IR}}-L_{\gamma}$ correlation adopted for the modeling of star-forming galaxies, etc.), which is inherently dangerous. Furthermore, we have illustrated in Sec. 6 how astrophysical uncertainties that manifest themselves as systematic shifts in averages-based methods typically also affect the shape of the one-point function when marginalised away in our distributional framework. Arguably one cannot address any astrophysical systematic self-consistently and distributionally, without incorporating the uncertainty directly into the model.

In the context of this study, we should not expect the statistical intricacies of one-point analyses to matter more than simply by changing the model to address the $\sim 5\sigma$, ~ 20 event mismatch between the model and the data (cf. Secs. 3.3.2 and 5.3). The existence of independent upper limits on the contributions of blazars and SFGs to the flux [26, 44, 62], that our models already saturate, suggest that it is premature to discuss upon the systematics of these subdominant contributions [16, 25, 53, 57, 59, 60]. Since we only aimed at proving the viability of our method through a simple modeling of the high-energy neutrino sky, other guaranteed sources of astrophysical neutrinos that can be well characterised using multimessenger data remain absent from the model.

In order to take into account the missing components of the neutrino flux predicted from our model, one could also consider nearby sources. While Galactic sources are a guaranteed contribution to the neutrino flux, they are not thought to be able to produce PeV neutrinos. However, the likelihood analysis above suggests that may not be necessary, and they can certainly generate neutrinos up to energies of a few hundred TeV (see, e.g., Ref. [11] for a summary of upper limits on Galactic contributions). Amongst other contributions, a phenomenological cosmic-ray model designed to reconcile *Fermi*, Milagro, and local cosmic-ray data, naturally predicts at least 10–20% of the IceCube flux [10], of the order of our count discrepancy. Whether the addition of this cosmic-ray contribution to the model is sufficient to explain the data, and a more systematic study of the model sensitivity to the various systematic uncertainties, is left to future work.

7 Conclusions

In this paper, for the first time, we explore the power of one-point statistical analyses in the context of neutrino astronomy. Such an analysis does not require point sources to be resolved in order to study properties of their population statistically, and, in this sense, it is intrinsically powerful when applied to contemporary high-energy neutrino data from the IceCube telescope.

We relied on data-driven models of only two extragalactic components (star-forming galaxies and blazars), besides the atmospheric neutrino flux, and compared our predictions with the IceCube detected flux [4]. The extragalactic neutrino backgrounds have been modeled by extrapolating multi-wavelength data from *Herschel* for the star-forming galaxy component [57] and from the *Fermi* 2FHL source catalogue for blazars [59, 60]. This study has yielded three main results.

Firstly, we quantified to what extent unresolved star-forming galaxies and blazars constitute *their own background* in dedicated IceCube point source searches. We showed that

if the neutrino flux of star-forming galaxies is well predicted from the *Herschel* data, then star-forming galaxies are likely to remain a diffuse, isotropic and featureless background for IceCube: only the diffuse peak of $P(F)$ can be probed. Note that our conclusions would be even more drastic if relying on more conservative estimates of the SFG neutrino contribution [42, 44]. This model-dependent claim is unequivocally demonstrated in showers, though in tracks we only place a conservative upper limit on the number $N_{\text{SFG}} \lesssim 25$ of resolvable sources at 100 TeV (a number to be revised in future studies due to other backgrounds and limited exposures). Our results are in agreement with the null results of dedicated point-source searches and cross-correlation studies [5, 17, 52, 86, 88]. The opposite is predicted for blazars: if the neutrino flux of this source population is well described by the 2FHL source catalogue, then these sources are rare enough that self-background effects are not relevant in tracks (see also the discussion in Ref. [20]). For both source populations, these model-dependent results are consistent with one-point fluctuation analyses in gamma-rays [51].

Secondly, the astrophysical distributions are found to be non-Gaussian with power-law tails. They are highly skewed, implying that IceCube observations are biased away from the mean. For rare sources, the most likely and mean values are predicted to be significantly different, by relative factors between 0.4 (showers) and 6.7 (tracks) in our blazar model. This weakens any upper limits on blazars based on the expected (mean) contributions of these populations to the isotropic flux in tracks, potentially by half an order of magnitude. The skewness of the star-forming galaxy distributions is much smaller, due to their larger abundance, therefore this effect is only percent-level.

Finally, we have applied one-point fluctuation and clustering analyses to neutrino data. Although these analyses are model-dependent, the models we have chosen are informed by (and otherwise consistent with) multimessenger data. We conclude in both analyses and with a high significance that this particular model cannot explain entirety of the IceCube neutrino events. This is not surprising, since we find (when correctly accounting for the skewness-induced bias) that blazars, star-forming galaxies and atmospheric foregrounds—all modeled as statistically isotropic components—contribute in total to less than two thirds of the HESE events. The likelihood analysis suggests that the discrepancy comes from either systematic uncertainties on the astrophysical components or new source populations whose spectra do not likely extend beyond 100 TeV. Given this result and the manifest power of these one-point methods, an extended study which takes into account more astrophysical uncertainties and more astrophysical source populations is desirable, as it will allow convergence (even without the need of more neutrino data) towards a multi-wavelength, data-driven, predictive model of the high-energy neutrino sky.

Acknowledgments

We thank Daniele Gaggero, Franca Hoffman, Felicia Krauss, Jakob van Santen, and Hannes Zechlin for useful discussions. This work was supported by the Netherlands Organisation for Scientific Research through Vidi grant. IT also acknowledges support from the Knud Højgaard Foundation, the Villum Foundation (Project No. 13164) and the Danish National Research Foundation (DNRF91).

A Modeling of the IceCube effective area

We want to compute (distributionally) the counts registered in a pixel due to a neutrino intensity $I_\nu = F_\nu/\Omega_{\text{pix}}$ incident on the detector. Given the distribution $P(I_\nu|E_\nu)$ of the

energy-differential intensity $I_\nu(E_\nu)$, and an energy-dependent effective area $A(E_\nu)$, we want to find the distribution $P(\mu_\nu)$ of the mean number of counts per pixel,

$$\mu_{\nu,\text{per pix}} = \int_{E_{\nu,\text{min}}}^{E_{\nu,\text{max}}} I_\nu(E_\nu) \Omega_{\text{pix}} A(E_\nu) t dE_\nu . \quad (\text{A.1})$$

In what follows, subscripts ν are suppressed for notational intelligibility.

A.1 Convolutional integration and neutrino fluxes

We can write the integral above as a Riemann sum, i.e.

$$\mu = \lim_{N \rightarrow \infty} \sum_{i=0}^{N-1} I(E + i\Delta E) A(E + i\Delta E) t \Omega \Delta E , \quad (\text{A.2})$$

where $\Delta E = (E_{\text{max}} - E_{\text{min}})/N$. We see that μ is a normalised sum $\mu = (X_0 + X_1 + \dots + X_{N-1})/N$ of an infinite number of random variables $X \sim IA\Omega t$, for which we might expect the central limit theorem (CLT) to hold. These X_i are not identically distributed (so the ‘‘classical’’ CLT does not work) but they are independent, so we might be able to use the Lyapunov CLT [91]. However it is easy to show that this extended CLT does not apply either (the Lyapunov Condition is violated for our power-law tailed distributions $P(I|E)$), i.e. that $P(\mu)$ need not to be Gaussian. Heuristically, if our Riemann sum is $\mu \sim (X_0 + X_1 + \dots + X_{N-1})$ then the distribution of this infinite sum is the infinite convolution

$$P(\mu) \sim \lim_{N \rightarrow \infty} \star_{i=0}^{N-1} P(X_i) , \quad (\text{A.3})$$

where we recall that $P(\dots)$ denotes a probability density function. See Figure 6 for a schematic of this convolution with $N = 4$.

Less informally, let $\mu = \int (X|E)dE$ denote an integrated conditional random variable (the ‘‘primitive function’’ or ‘‘antiderivative’’ of the conditional variable $X|E \in \mathbb{R}^+$ with respect to the random variable E). For our purposes, the probability distribution function of E need not be specified beyond the fact that two fixed limits of integration \mathcal{E}_{min} and \mathcal{E}_{max} live within the support of $P(E)$. We can then express the distribution function $P(\mu)$ as

$$P(\mu|\mathcal{E}_{\text{min}} \leq E < \mathcal{E}_{\text{max}}) = \lim_{N \rightarrow \infty} \star_{i=0}^{N-1} \left[\delta \left(\mu - \sum_{j=0}^{N-1} X_j \right) P(X_i | E = \mathcal{E}_{\text{min}} + i\Delta\mathcal{E}) \right] , \quad (\text{A.4})$$

where $\Delta\mathcal{E} = (\mathcal{E}_{\text{max}} - \mathcal{E}_{\text{min}})/N$ and where $\delta(\mu - \sum X)$ enforces the Riemann sum on the independent summands X_i . This expression of course follows from the marginalisation of

$$P(\mu, X_0, \dots, X_{N-1}) = P(\mu|X_0, \dots, X_{N-1})P(X_0) \dots P(X_{N-1}), \quad (\text{A.5})$$

with $P(\mu|X\text{'s}) = \delta(\mu - \sum X)$ and $N \rightarrow \infty$. A formal definition and study of this operation (presumably in terms of the Itô-Stratonovic stochastic integral [92]) is left to future work, in what follows we adopt physically motivated assumptions in order to compute it. Also, it will be clearer to condense this limit of many convolutions into the notation

$$P(\mu|\mathcal{E}_{\text{min}} \leq E < \mathcal{E}_{\text{max}}) \equiv \star_{\mathcal{E}_{\text{min}}}^{\mathcal{E}_{\text{max}}} P(X|E)dE . \quad (\text{A.6})$$

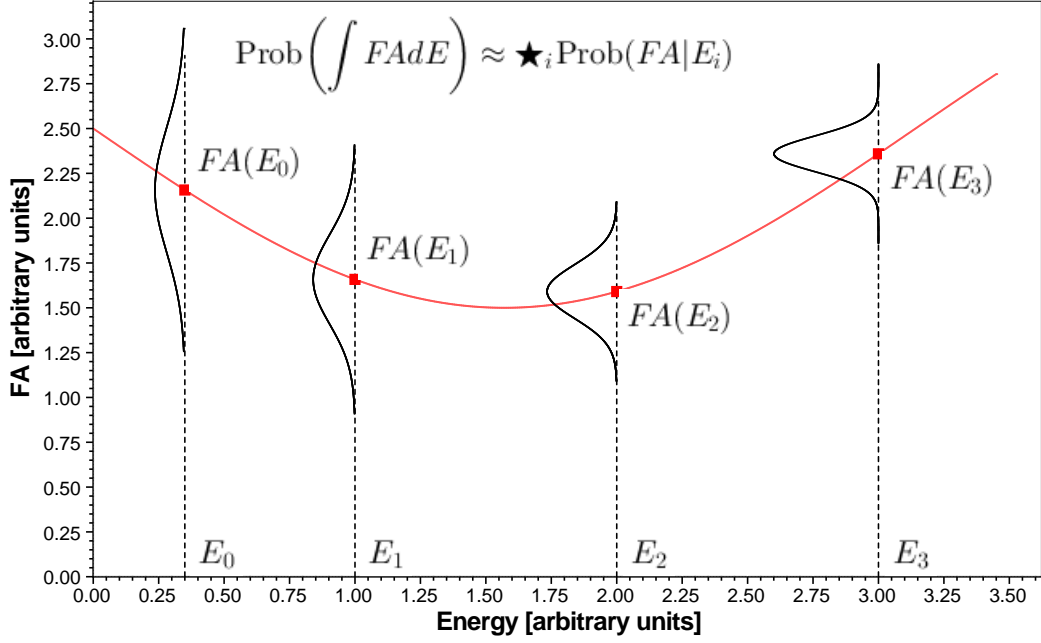


Figure 6: Schematic of the integration of a conditional random variable. Specifically, this illustrates the computation of the mean-count distribution $P(\mu)$, where $\mu = \int F_\nu AT dE_\nu$ with T constant and $F_\nu = I_\nu \Omega$. Since integrals look like sums, the probability distribution of an integrated quantity is the convolution of the distributions of the integrand as a function of the variable of integration.

Although this quantity is mathematically interesting, in practice we can not compute a number $N \rightarrow \infty$ of convolutions. Since convolution is associative, convolutive integration is composable in its boundaries:

$$\star_a^c P(F|E)dE = \left(\star_a^b P(F|E)dE \right) \star \left(\star_b^c P(F|E)dE \right). \quad (\text{A.7})$$

Using this property and working with integrated fluxes $S = \int FdE$, we can approximate the convolutive integral of differential fluxes as the convolution of integrated fluxes:

$$\star_{\Delta E} P(F|E)dE \approx \star_{i=0}^{N-1} P(S|\delta E_i). \quad (\text{A.8})$$

This *distributionally* reproduces the insight (conveyed in the main text) that the flux S is an extensive quantity (with respect to E), so that the flux over a sum of bins is the sum of the fluxes in each bin $S(\Delta E) = \sum_i S(\delta E_i)$. With this understanding, we can finally compute

$$P(\mu|\Delta E) \approx \star_{i=0}^{N-1} P(S_i \times A_i \times t | \delta E_i), \quad (\text{A.9})$$

where the number of convolutions is chosen large enough that $A(E)$ can be treated as a constant A_i in each subbin δE_i .

A.2 Declination dependence

In addition to this energy-dependence, note that the effective area is also declination dependent. In our analysis we simply use the central declination of each pixel to compute $A(E)$. For showers, HealPix [73] generates pixels at seven different latitudes, calling for seven computations of $P(C)$ for each source class, for each of the two event topologies, and for each of the three energy bins. For tracks, HealPix generates 255 different latitudes. To facilitate comparisons we compute $P(C)$ at the same seven latitudes as for showers and use whichever declination is closest. This is particularly relevant for our discussion of clustering in Sec. 4.2, where the distributions in tracks were coarse-grained to the scale of showers by autoconvolution. This shortcut can only be exploited if we restrict ourselves to components with at most iso-latitudinal variations such as (to a good approximation) the atmospheric component [66]. A dedicated analysis of truly anisotropic components, such as the neutrino contribution of the Galactic plane [10], is left to future work.

A.3 Flavour dependence

IceCube provides a separate estimation of the effective area for each of the three flavours, which we interpolate in declination and energy in order to use the formalism above. However, the effective area for tracks and showers depends on the probability $p_{T/S}^{e/\mu/\tau}$ that a neutrino of a given flavour (sampled randomly from the total neutrino flux) produces a charged or a neutral current interaction in the ice. We use the approximation [72]

$$\{p_T^\mu = 0.8, p_S^\mu = 0.2, p_S^{e/\tau} = 1, p_T^{e/\tau} = 0\} \quad (\text{A.10})$$

to write

$$A_{T/S} = 2 \sum_{f \in \{e, \mu, \tau\}} p_{T/S}^f \times A^f \times \eta^f, \quad (\text{A.11})$$

where A^f is the flavour-energy-and-declination dependent quantity given by IceCube [2] and η^f is the fraction of neutrinos of a given flavour ($\eta = 1/3$ for a 1 : 1 : 1 flavour ratio). We multiply the effective area by 2 since the sum does not run over antineutrinos, effectively setting equal neutrino and antineutrino fluxes. We employ a 1 : 1 : 1 ratio for all extragalactic components, a 0 : 1 : 0 flavour ratio for the conventional atmospheric flux, and a 1 : 1 : 0 ratio for the prompt atmospheric flux [67]. Percent-level atmospheric contributions from ν_e and ν_τ fluxes (respectively) [66, 67] are neglected, as are the neutrino-antineutrino ratios, although the fully detailed (even energy-dependent) flavour ratios can manifestly be accounted for in this type of analysis.

B Methodological contrast to one-point fitting

One-point methods, pioneered and refined by $P(D)$ analysis [74–76], are currently experiencing a rebirth in contemporary astrophysics [46–51, 93–99]. The objective of such methods is typically to fit the resolved and unresolved point source distribution dN/dF to the data in terms of a phenomenological model, to be interpreted after the conclusion of the analysis proper. In gamma-rays, for example, the generating function approach in Ref. [47] was for this purpose considerably enhanced, with careful studies of the dN/dF prior-dependence [50, 94] and systematics [51] of the fitting procedure. Both the generating-function-fitting method and the distribution-modelling method in the present study essentially require (i) an

ansatz on the source count distribution,¹⁰ (ii) a model of the response of the instrument to incident flux, and (iii) a way to transition from one to the other.

The two approaches are most obviously distinguished by this third point, particularly by the direction of this transition (from model to prediction / from data to fit) and by its nature (a probabilistic hierarchical network / use of a specific statistical estimator). A perhaps more subtle distinction between the two methods is that one can model the flux distribution of many source populations in many detectors, while the specific estimator adopted in the fitting method is (at least in its current form) one-to-one. The main text illustrates the multiplicity of source populations, with different abundances, spectral indices and redshift evolutions; but besides IceCube, all instruments sensitive to high-energy neutrinos currently produce non-measurements [100–102]. And although in this study we restrict our attention to neutrino data at the highest energies, a one-point analysis can in principle be both multi-wavelength and multi-messenger, if the model \mathbf{M} of astrophysics and of instrument responses that gives rise to the $P(C|\mathbf{M})$ count distributions is sufficiently elaborate.

In gamma-rays, there is enough data that the choice between the two methods is to a large extent a matter of taste. However, a generating-function analysis would be ill-suited to the low statistics of contemporary high-energy IceCube data: such an analysis is blind to features below the single-event sensitivity [50]. One should expect that the experimental event count distribution is too poorly sampled to drive significant fits of the source count distribution. Even if it were not, it would *by design* be incapable of disentangling the subdominant source population contributions from its unique dN/dF : any post-hoc interpretation of such a poorly-fit dN/dF would live in a limbo of untested conjectures in wait of more data.

By contrast, in the modelling approach, various hypothetical combinations of flux distributions can be tested against the neutrino data, e.g. in terms of a likelihood ratio / Bayes factor. When they fail to be rejected by the data, or when preferences between multiple models fail to emerge significantly from the data, this occurs formally and quantifiably. On the other hand, when a model is rejected by the data, and hypotheses for this failure are put forward (in our case, the hypothesis that there is a contribution missing), these are *guaranteed to be testable with contemporary data* (by improvement of the model and re-analysis). These model improvements and tests are not a methodological shortcoming, but indeed an opportunity to be explored in future work.

References

- [1] **IceCube** Collaboration, M. G. Aartsen et al., *First observation of PeV-energy neutrinos with IceCube*, *Phys. Rev. Lett.* **111** (2013) 021103, [[arXiv:1304.5356](#)].
- [2] **IceCube** Collaboration, M. G. Aartsen et al., *Evidence for High-Energy Extraterrestrial Neutrinos at the IceCube Detector*, *Science* **342** (2013) 1242856, [[arXiv:1311.5238](#)].
- [3] **IceCube** Collaboration, M. G. Aartsen et al., *Observation of High-Energy Astrophysical Neutrinos in Three Years of IceCube Data*, *Phys. Rev. Lett.* **113** (2014) 101101, [[arXiv:1405.5303](#)].
- [4] **IceCube** Collaboration, C. Kopper, W. Giang, N. Kurahashi, et al., *Observation of astrophysical neutrinos in four years of icecube data*, in *PoS (ICRC2015) 1081*, 2015.
- [5] **IceCube** Collaboration, M. G. Aartsen et al., *All-sky search for time-integrated neutrino emission from astrophysical sources with 7 years of IceCube data*, [arXiv:1609.04981](#).

¹⁰In the generating-function approach, this is an ansatz on the parameterisation of dN/dF and on the priors associated to the parameter values.

- [6] L. A. Anchordoqui et al., *Cosmic Neutrino Pevatrons: A Brand New Pathway to Astronomy, Astrophysics, and Particle Physics*, *JHEAp* **1-2** (2014) 1–30, [[arXiv:1312.6587](#)].
- [7] **IceCube** Collaboration, M. G. Aartsen et al., *Searches for small-scale anisotropies from neutrino point sources with three years of IceCube data*, *Astropart. Phys.* **66** (2015) 39–52, [[arXiv:1408.0634](#)].
- [8] A. Neronov and D. V. Semikoz, *Evidence the Galactic contribution to the IceCube astrophysical neutrino flux*, *Astropart. Phys.* **75** (2016) 60–63, [[arXiv:1509.03522](#)].
- [9] M. Leuermann, M. Schimp, and C. H. Wiebusch, *Astrophysical interpretation of small-scale neutrino angular correlation searches with IceCube*, *Astropart. Phys.* **83** (2016) 21–29, [[arXiv:1603.01385](#)].
- [10] D. Gaggero, D. Grasso, A. Marinelli, A. Urbano, and M. Valli, *The gamma-ray and neutrino sky: A consistent picture of Fermi-LAT, Milagro, and IceCube results*, *Astrophys. J.* **815** (2015), no. 2 L25, [[arXiv:1504.00227](#)].
- [11] M. Ahlers and K. Murase, *Probing the Galactic Origin of the IceCube Excess with Gamma-Rays*, *Phys. Rev.* **D90** (2014), no. 2 023010, [[arXiv:1309.4077](#)].
- [12] A. Loeb and E. Waxman, *The cumulative background of high energy neutrinos from starburst galaxies*, *Journal of Cosmology and Astro-Particle Physics* **5** (2006) [[astro-ph/0601695](#)].
- [13] H.-N. He, T. Wang, Y.-Z. Fan, S.-M. Liu, and D.-M. Wei, *Diffuse PeV neutrino emission from ultraluminous infrared galaxies*, *Phys. Rev.* **D87** (2013), no. 6 063011, [[arXiv:1303.1253](#)].
- [14] R.-Y. Liu, X.-Y. Wang, S. Inoue, R. Crocker, and F. Aharonian, *Diffuse PeV neutrinos from EeV cosmic ray sources: Semirelativistic hypernova remnants in star-forming galaxies*, *Phys. Rev.* **D89** (2014), no. 8 083004, [[arXiv:1310.1263](#)].
- [15] K. Murase, M. Ahlers, and B. Lacki, *Testing the hadronuclear origin of peV neutrinos observed with icecube*, *Physical Review D* **88** (2013), no. 12 [[arXiv:1306.3417](#)].
- [16] I. Tamborra, S. Ando, and K. Murase, *Star-forming galaxies as the origin of diffuse high-energy backgrounds: Gamma-ray and neutrino connections, and implications for starburst history*, *JCAP* **1409** (2014), no. 09 043, [[arXiv:1404.1189](#)].
- [17] L. A. Anchordoqui, T. C. Paul, L. H. M. da Silva, D. F. Torres, and B. J. Vlcek, *What IceCube data tell us about neutrino emission from star-forming galaxies (so far)*, *Phys. Rev.* **D89** (2014), no. 12 127304, [[arXiv:1405.7648](#)].
- [18] S. Chakraborty and I. Izaguirre, *Diffuse neutrinos from extragalactic supernova remnants: Dominating the 100 TeV IceCube flux*, *Phys. Lett.* **B745** (2015) 35–39, [[arXiv:1501.02615](#)].
- [19] N. Senno, P. Mészáros, K. Murase, P. Baerwald, and M. J. Rees, *Extragalactic star-forming galaxies with hypernovae and supernovae as high-energy neutrino and gamma-ray sources: the case of the 10 TeV neutrino data*, *Astrophys. J.* **806** (2015), no. 1 24, [[arXiv:1501.04934](#)].
- [20] M. Kadler et al., *Coincidence of a high-fluence blazar outburst with a PeV-energy neutrino event*, *Nature Phys.* **12** (2016), no. 8 807–814, [[arXiv:1602.02012](#)].
- [21] O. E. Kalashev, A. Kusenko, and W. Essey, *PeV neutrinos from intergalactic interactions of cosmic rays emitted by active galactic nuclei*, *Phys. Rev. Lett.* **111** (2013), no. 4 041103, [[arXiv:1303.0300](#)].
- [22] F. W. Stecker, *PeV neutrinos observed by IceCube from cores of active galactic nuclei*, *Phys. Rev.* **D88** (2013), no. 4 047301, [[arXiv:1305.7404](#)].
- [23] K. Murase, Y. Inoue, and C. D. Dermer, *Diffuse Neutrino Intensity from the Inner Jets of Active Galactic Nuclei: Impacts of External Photon Fields and the Blazar Sequence*, *Phys. Rev.* **D90** (2014), no. 2 023007, [[arXiv:1403.4089](#)].
- [24] C. D. Dermer, K. Murase, and Y. Inoue, *Photopion Production in Black-Hole Jets and*

- Flat-Spectrum Radio Quasars as PeV Neutrino Sources*, *JHEAp* **3-4** (2014) 29–40, [[arXiv:1406.2633](#)].
- [25] P. Padovani, M. Petropoulou, P. Giommi, and E. Resconi, *A simplified view of blazars: the neutrino background*, *Mon. Not. Roy. Astron. Soc.* **452** (2015), no. 2 1877–1887, [[arXiv:1506.09135](#)].
- [26] B. Wang and Z. Li, *Can FSRQs produce the IceCube detected diffuse neutrino emission?*, *Sci. China Phys. Mech. Astron.* **59** (2016), no. 1 619502, [[arXiv:1505.04418](#)].
- [27] D. Hooper, *A Case for Radio Galaxies as the Sources of IceCube’s Astrophysical Neutrino Flux*, *JCAP* **1609** (2016), no. 09 002, [[arXiv:1605.06504](#)].
- [28] P. Padovani, E. Resconi, P. Giommi, B. Arsioli, and Y. L. Chang, *Extreme blazars as counterparts of IceCube astrophysical neutrinos*, *Mon. Not. Roy. Astron. Soc.* **457** (2016), no. 4 3582–3592, [[arXiv:1601.06550](#)].
- [29] K. Murase and J. F. Beacom, *Galaxy Clusters as Reservoirs of Heavy Dark Matter and High-Energy Cosmic Rays: Constraints from Neutrino Observations*, *JCAP* **1302** (2013) 028, [[arXiv:1209.0225](#)].
- [30] F. Zandanel, I. Tamborra, S. Gabici, and S. Ando, *High-energy gamma-ray and neutrino backgrounds from clusters of galaxies and radio constraints*, *Astron. Astrophys.* **578** (2015) A32, [[arXiv:1410.8697](#)].
- [31] K. Murase and K. Ioka, *TeV-PeV Neutrinos from Low-Power Gamma-Ray Burst Jets inside Stars*, *Phys. Rev. Lett.* **111** (2013), no. 12 121102, [[arXiv:1306.2274](#)].
- [32] R.-Y. Liu and X.-Y. Wang, *Diffuse PeV neutrinos from gamma-ray bursts*, *Astrophys. J.* **766** (2013) 73, [[arXiv:1212.1260](#)].
- [33] I. Tamborra and S. Ando, *Diffuse emission of high-energy neutrinos from gamma-ray burst fireballs*, *JCAP* **1509** (2015), no. 09 036, [[arXiv:1504.00107](#)].
- [34] I. Tamborra and S. Ando, *Inspecting the supernova?gamma-ray-burst connection with high-energy neutrinos*, *Phys. Rev.* **D93** (2016), no. 5 053010, [[arXiv:1512.01559](#)].
- [35] N. Senno, K. Murase, and P. Meszaros, *Choked Jets and Low-Luminosity Gamma-Ray Bursts as Hidden Neutrino Sources*, *Phys. Rev.* **D93** (2016), no. 8 083003, [[arXiv:1512.08513](#)].
- [36] Y. Fujita, S. S. Kimura, and K. Murase, *Hadronic origin of multi-TeV gamma rays and neutrinos from low-luminosity active galactic nuclei: Implications of past activities of the Galactic center*, *Phys. Rev.* **D92** (2015), no. 2 023001, [[arXiv:1506.05461](#)].
- [37] S. S. Kimura, K. Murase, and K. Toma, *Neutrino and Cosmic-Ray Emission and Cumulative Background from Radiatively Inefficient Accretion Flows in Low-Luminosity Active Galactic Nuclei*, *Astrophys. J.* **806** (2015) 159, [[arXiv:1411.3588](#)].
- [38] B. Feldstein, A. Kusenko, S. Matsumoto, and T. T. Yanagida, *Neutrinos at IceCube from Heavy Decaying Dark Matter*, *Phys. Rev.* **D88** (2013), no. 1 015004, [[arXiv:1303.7320](#)].
- [39] A. Esmaili and P. D. Serpico, *Are IceCube neutrinos unveiling PeV-scale decaying dark matter?*, *JCAP* **1311** (2013) 054, [[arXiv:1308.1105](#)].
- [40] J. Zavala, *Galactic PeV neutrinos from dark matter annihilation*, *Phys. Rev.* **D89** (2014), no. 12 123516, [[arXiv:1404.2932](#)].
- [41] K. Murase, R. Laha, S. Ando, and M. Ahlers, *Testing the Dark Matter Scenario for PeV Neutrinos Observed in IceCube*, *Phys. Rev. Lett.* **115** (2015), no. 7 071301, [[arXiv:1503.04663](#)].
- [42] S. Ando, I. Tamborra, and F. Zandanel, *Tomographic Constraints on High-Energy Neutrinos of Hadronuclear Origin*, *Phys. Rev. Lett.* **115** (2015), no. 22 221101, [[arXiv:1509.02444](#)].

- [43] K. Murase and E. Waxman, *Constraining High-Energy Cosmic Neutrino Sources: Implications and Prospects*, *Phys. Rev.* **D94** (2016), no. 10 103006, [[arXiv:1607.01601](#)].
- [44] K. Bechtol, M. Ahlers, M. Di Mauro, M. Ajello, and J. Vandenbroucke, *Evidence against star-forming galaxies as the dominant source of IceCube neutrinos*, [arXiv:1511.00688](#).
- [45] K. Murase, D. Guetta, and M. Ahlers, *Hidden Cosmic-Ray Accelerators as an Origin of TeV-PeV Cosmic Neutrinos*, *Phys. Rev. Lett.* **116** (2016), no. 7 071101, [[arXiv:1509.00805](#)].
- [46] M. R. Feyereisen, S. Ando, and S. K. Lee, *Modelling the flux distribution function of the extragalactic gamma-ray background from dark matter annihilation*, *JCAP* **1509** (2015), no. 09 027, [[arXiv:1506.05118](#)].
- [47] D. Malyshev and D. W. Hogg, *Statistics of gamma-ray point sources below the Fermi detection limit*, *Astrophys. J.* **738** (2011) 181, [[arXiv:1104.0010](#)].
- [48] S. K. Lee, S. Ando, and M. Kamionkowski, *The Gamma-Ray-Flux Probability Distribution Function from Galactic Halo Substructure*, *JCAP* **0907** (2009) 007, [[arXiv:0810.1284](#)].
- [49] S. K. Lee, M. Lisanti, B. R. Safdi, T. R. Slatyer, and W. Xue, *Evidence for Unresolved γ -Ray Point Sources in the Inner Galaxy*, *Phys. Rev. Lett.* **116** (2016), no. 5 051103, [[arXiv:1506.05124](#)].
- [50] H.-S. Zechlin, A. Cuoco, F. Donato, N. Fornengo, and A. Vittino, *Unveiling the Gamma-ray Source Count Distribution Below the Fermi Detection Limit with Photon Statistics*, *Astrophys. J. Suppl.* **225** (2016), no. 2 18, [[arXiv:1512.07190](#)].
- [51] M. Lisanti, S. Mishra-Sharma, L. Necib, and B. R. Safdi, *Deciphering Contributions to the Extragalactic Gamma-Ray Background from 2 GeV to 2 TeV*, *Astrophys. J.* **832** (2016), no. 2 117, [[arXiv:1606.04101](#)].
- [52] M. Ahlers and F. Halzen, *Pinpointing Extragalactic Neutrino Sources in Light of Recent IceCube Observations*, *Phys. Rev.* **D90** (2014), no. 4 043005, [[arXiv:1406.2160](#)].
- [53] **Fermi-LAT** Collaboration, M. Ackermann et al., *GeV Observations of Star-forming Galaxies with Fermi LAT*, *Astrophys. J.* **755** (2012) 164, [[arXiv:1206.1346](#)].
- [54] Q.-W. Tang, X.-Y. Wang, and P.-H. T. Tam, *Discovery of gev emission from the direction of the luminous infrared galaxy ngc 2146*, [arXiv:1407.3391](#).
- [55] F.-K. Peng, X.-Y. Wang, R.-Y. Liu, Q.-W. Tang, and J.-F. Wang, *First detection of GeV emission from an ultraluminous infrared galaxy: Arp 220 as seen with the Fermi Large Area Telescope*, *Astrophys. J.* **821** (2016), no. 2 L20, [[arXiv:1603.06355](#)].
- [56] **Fermi-LAT** Collaboration, F. Acero et al., *Fermi Large Area Telescope Third Source Catalog*, *Astrophys. J. Suppl.* **218** (2015), no. 2 23, [[arXiv:1501.02003](#)].
- [57] C. Gruppioni et al., *The Herschel PEP/HerMES Luminosity Function. I: Probing the Evolution of PACS selected Galaxies to z 4*, *Mon. Not. Roy. Astron. Soc.* **432** (2013) 23, [[arXiv:1302.5209](#)].
- [58] **Planck** Collaboration, P. Ade et al., *Planck 2013 results. XVI. Cosmological parameters*, *Astron. Astrophys.* **571** (2014) A16, [[arXiv:1303.5076](#)].
- [59] **Fermi-LAT** Collaboration, M. Ackermann et al., *2FHL: The Second Catalog of Hard Fermi-LAT Sources*, *Astrophys. J. Suppl.* **222** (2016), no. 1 5, [[arXiv:1508.04449](#)].
- [60] **Fermi-LAT** Collaboration, M. Ackermann, M. Ajello, et al., *Resolving the extragalactic gamma-ray background above 50 gev with fermi-lat*, *arXiv* (2015) [[1511.00693](#)].
- [61] **Fermi-LAT** Collaboration, M. Ackermann, M. Ajello, A. Allafort, E. Antolini, W. Atwood, M. Axelsson, L. Baldini, J. Ballet, G. Barbiellini, D. Bastieri, et al., *The second catalog of active galactic nuclei detected by the fermi large area telescope*, *The Astrophysical Journal* **743** (2011), no. 2 171, [[arXiv:1108.1420](#)].

- [62] **IceCube** Collaboration, T. Glüsenkamp, *Analysis of the cumulative neutrino flux from Fermi-LAT blazar populations using 3 years of IceCube data*, *EPJ Web Conf.* **121** (2016) 05006, [[arXiv:1502.03104](#)].
- [63] **IceCube** Collaboration, M. G. Aartsen et al., *Atmospheric and astrophysical neutrinos above 1 TeV interacting in IceCube*, *Phys. Rev.* **D91** (2015), no. 2 022001, [[arXiv:1410.1749](#)].
- [64] S. Dimitrakoudis, M. Petropoulou, and A. Mastichiadis, *Self-consistent neutrino and UHE cosmic ray spectra from Mrk 421*, *Astropart. Phys.* **54** (2014) 61–66, [[arXiv:1310.7923](#)].
- [65] M. Petropoulou, S. Dimitrakoudis, P. Padovani, A. Mastichiadis, and E. Resconi, *Photohadronic origin of gamma-ray BL Lac emission: implications for IceCube neutrinos*, *Mon. Not. Roy. Astron. Soc.* **448** (2015), no. 3 2412–2429, [[arXiv:1501.07115](#)].
- [66] M. Honda, M. Sajjad Athar, T. Kajita, K. Kasahara, and S. Midorikawa, *Atmospheric neutrino flux calculation using the NRLMSISE-00 atmospheric model*, *Phys. Rev.* **D92** (2015), no. 2 023004, [[arXiv:1502.03916](#)].
- [67] R. Enberg, M. H. Reno, and I. Sarcevic, *Prompt neutrino fluxes from atmospheric charm*, *Phys. Rev.* **D78** (2008) 043005, [[arXiv:0806.0418](#)].
- [68] F. Halzen and L. Wille, *Upper Limit on Forward Charm Contribution to Atmospheric Neutrino Flux*, [arXiv:1601.03044](#).
- [69] R. Laha and S. J. Brodsky, *IC at IC: IceCube can constrain the intrinsic charm of the proton*, [arXiv:1607.08240](#).
- [70] A. Bhattacharya, R. Enberg, Y. S. Jeong, C. S. Kim, M. H. Reno, I. Sarcevic, and A. Stasto, *Prompt atmospheric neutrino fluxes: perturbative QCD models and nuclear effects*, *JHEP* **11** (2016) 167, [[arXiv:1607.00193](#)].
- [71] **IceCube** Collaboration, M. G. Aartsen et al., *A combined maximum-likelihood analysis of the high-energy astrophysical neutrino flux measured with IceCube*, *Astrophys. J.* **809** (2015), no. 1 98, [[arXiv:1507.03991](#)].
- [72] A. Palladino, G. Pagliaroli, F. L. Villante, and F. Vissani, *What is the Flavor of the Cosmic Neutrinos Seen by IceCube?*, *Phys. Rev. Lett.* **114** (2015), no. 17 171101, [[arXiv:1502.02923](#)].
- [73] K. M. Gorski, E. Hivon, A. J. Banday, B. D. Wandelt, F. K. Hansen, M. Reinecke, and M. Bartelman, *Healpix – a framework for high resolution discretization, and fast analysis of data distributed on the sphere*, [astro-ph/0409513](#).
- [74] P. A. Scheuer, *A statistical method for analysing observations of faint radio stars*, in *Mathematical Proceedings of the Cambridge Philosophical Society*, vol. 53, pp. 764–773, Cambridge Univ Press, 1957.
- [75] X. Barcons, *Confusion noise and source clustering*, *The Astrophysical Journal* **396** (1992) 460–468.
- [76] X. Barcons, G. Branduardi-Raymont, R. S. Warwick, A. C. Fabian, K. O. Mason, I. McHardy, and M. Rowan-Robinson, *Deep x-ray source counts from a fluctuation analysis of rosat pspc images*, *Monthly Notices of the Royal Astronomical Society* **268** (1994), no. 4 833–840, [<http://mnras.oxfordjournals.org/content/268/4/833.full.pdf+html>].
- [77] **IceCube** Collaboration, M. G. Aartsen et al., *Energy Reconstruction Methods in the IceCube Neutrino Telescope*, *JINST* **9** (2014) P03009, [[arXiv:1311.4767](#)].
- [78] A. C. Cohen, *Estimating the mean and variance of normal populations from singly truncated and doubly truncated samples*, *Ann. Math. Statist.* **21** (12, 1950) 557–569.
- [79] R. Bartels, S. Krishnamurthy, and C. Weniger, *Strong support for the millisecond pulsar origin of the Galactic center GeV excess*, *Phys. Rev. Lett.* **116** (2016), no. 5 051102, [[arXiv:1506.05104](#)].

- [80] **KM3NeT** Collaboration, S. Adrián-Martínez, M. Ageron, F. Aharonian, et al., *Letter of intent for km³net 2.0*, [arXiv:1601.07459](https://arxiv.org/abs/1601.07459).
- [81] M. Aartsen, M. Ackermann, J. Adams, J. Aguilar, M. Ahlers, M. Ahrens, D. Altmann, T. Anderson, G. Anton, C. Argüelles, et al., *IceCube-Gen2: a vision for the future of neutrino astronomy in antarctica*, [arXiv:1412.5106](https://arxiv.org/abs/1412.5106).
- [82] **IceCube** Collaboration, D. F. Cowen, *Tau neutrinos in IceCube*, *J. Phys. Conf. Ser.* **60** (2007) 227–230.
- [83] **IceCube** Collaboration, M. G. Aartsen et al., *Search for Astrophysical Tau Neutrinos in Three Years of IceCube Data*, *Phys. Rev.* **D93** (2016), no. 2 022001, [[arXiv:1509.06212](https://arxiv.org/abs/1509.06212)].
- [84] S. Goodman, *Aligning statistical and scientific reasoning*, *Science* **352** (2016), no. 6290 1180–1181.
- [85] J. D. Gibbons and J. W. Pratt, *P-values: Interpretation and methodology*, *The American Statistician* **29** (1975), no. 1 20–25, [<http://dx.doi.org/10.1080/00031305.1975.10479106>].
- [86] K. Emig, C. Lunardini, and R. Windhorst, *Do high energy astrophysical neutrinos trace star formation?*, *JCAP* **1512** (2015) 029, [[arXiv:1507.05711](https://arxiv.org/abs/1507.05711)].
- [87] K. Fang, K. Kotera, M. C. Miller, K. Murase, and F. Oikonomou, *Identifying Ultrahigh-Energy Cosmic-Ray Accelerators with Future Ultrahigh-Energy Neutrino Detectors*, *JCAP* **1612** (2016), no. 12 017, [[arXiv:1609.08027](https://arxiv.org/abs/1609.08027)].
- [88] R. Moharana and S. Razzaque, *Angular correlation between IceCube high-energy starting events and starburst sources*, *JCAP* **1612** (2016) 021, [[arXiv:1606.04420](https://arxiv.org/abs/1606.04420)].
- [89] P. Padovani and E. Resconi, *Are both BL Lacs and pulsar wind nebulae the astrophysical counterparts of IceCube neutrino events?*, *Mon. Not. Roy. Astron. Soc.* **443** (2014), no. 1 474–484, [[arXiv:1406.0376](https://arxiv.org/abs/1406.0376)].
- [90] M. Yang, *Normal log-normal mixture, leptokurtosis and skewness*, *Applied Economics Letters* **15** (2008), no. 9 737–742, [<http://www.tandfonline.com/doi/pdf/10.1080/13504850600749073>].
- [91] V. V. Petrov, *Sums of independent random variables*, vol. 82. Springer, 1975.
- [92] M. Tai, *A mathematical model for the determination of total area under glucose tolerance and other metabolic curves*, *Diabetes Care* **17** (1994), no. 2 152–154.
- [93] J. Glenn, A. Conley, M. Béthermin, et al., *Hermes: deep galaxy number counts from a $p(d)$ fluctuation analysis of spire science demonstration phase observations*, *Monthly Notices of the Royal Astronomical Society* **409** (2010), no. 1 109–121, [<http://mnras.oxfordjournals.org/content/409/1/109.full.pdf+html>].
- [94] H.-S. Zechlin, A. Cuoco, F. Donato, N. Fornengo, and M. Regis, *Statistical Measurement of the Gamma-ray Source-count Distribution as a Function of Energy*, *Astrophys. J.* **826** (2016), no. 2 L31, [[arXiv:1605.04256](https://arxiv.org/abs/1605.04256)].
- [95] J. J. Condon, W. D. Cotton, E. B. Fomalont, K. I. Kellermann, N. Miller, R. A. Perley, D. Scott, T. Vernstrom, and J. V. Wall, *Resolving the Radio Source Background: Deeper Understanding Through Confusion*, *Astrophys. J.* **758** (2012) 23, [[arXiv:1207.2439](https://arxiv.org/abs/1207.2439)].
- [96] T. Vernstrom, D. Scott, J. V. Wall, J. J. Condon, W. D. Cotton, E. B. Fomalont, K. I. Kellermann, N. Miller, and R. A. Perley, *Deep 3 GHz number counts from a $P(D)$ fluctuation analysis*, *Mon. Not. Roy. Astron. Soc.* **440** (2014), no. 3 2791–2809, [[arXiv:1311.7451](https://arxiv.org/abs/1311.7451)].
- [97] P. C. Breyse, E. D. Kovetz, and M. Kamionkowski, *Carbon monoxide intensity mapping at moderate redshifts*, *Monthly Notices of the Royal Astronomical Society* **443** (2014), no. 4 3506–3512, [<http://mnras.oxfordjournals.org/content/443/4/3506.full.pdf+html>].

- [98] P. C. Breysse, E. D. Kovetz, and M. Kamionkowski, *The high-redshift star formation history from carbon-monoxide intensity maps*, *Monthly Notices of the Royal Astronomical Society: Letters* **457** (2016), no. 1 L127–L131, [<http://mnrasl.oxfordjournals.org/content/457/1/L127.full.pdf+html>].
- [99] P. C. Breysse, E. D. Kovetz, P. S. Behroozi, L. Dai, and M. Kamionkowski, *Insights from probability distribution functions of intensity maps*, [arXiv:1609.01728](https://arxiv.org/abs/1609.01728).
- [100] **Pierre Auger** Collaboration, P. Abreu et al., *Ultra-high Energy Neutrinos at the Pierre Auger Observatory*, *Adv. High Energy Phys.* **2013** (2013) 708680, [[arXiv:1304.1630](https://arxiv.org/abs/1304.1630)].
- [101] P. W. Gorham et al., *Observational constraints on the ultra-high energy cosmic neutrino flux from the second flight of the anita experiment*, *Physical Review D* **82** (2010), no. 2 [[1003.2961](https://arxiv.org/abs/1003.2961)].
- [102] P. W. Gorham et al., *Erratum: Observational constraints on the ultra-high energy cosmic neutrino flux from the second flight of the anita experiment [phys. rev. d, 82, 022004 (2010)]*, *Physical Review D* **85** (2012), no. 4 [[1011.5004](https://arxiv.org/abs/1011.5004)].